Protostellar jets and planet-forming disks: Witnessing the formation of Solar System analogues with interferometry

Tychoniec, Ł.

5

Which molecule traces what: chemical diagnostics of protostellar sources

Tychoniec Ł., van Dishoeck E. F., van ’t Hoff M. L. R., van Gelder M. L., Tabone B., Chen Y., Harsono D., Hull C. L. H., Hogerheijde M. R., Murillo N. M., Tobin J. J.
Submitted to Astronomy & Astrophysics.

Abstract

The physical and chemical conditions in Class 0/I protostars are fundamental in unlocking the protostellar accretion process and its impact on planet formation. The aim is to determine which physical components are traced by different molecules at sub-arcsecond scales (<100 − 400 au). We use a suite of Atacama Large Millimeter/submillimeter Array (ALMA) datasets in Band 6 (1 mm), Band 5 (1.8 mm) and Band 3 (3 mm) at spatial resolutions 0.″5 − 3″for 16 protostellar sources. For a subset of sources, Atacama Compact Array (ACA) data at Band 6 with a spatial resolution of 6″ are added. The availability of both low- and high-excitation lines, as well as data on small and larger scales, are important to unravel the full picture. The quiescent protostellar envelope is well traced by $C^{18}O$, DCO^+ and N_2D^+, with the freeze-out of CO governing the chemistry at envelope scales. Molecular outflows are seen in classical shock tracers like SiO and SO, but ice-mantle products such as CH_3OH and HNCO released with the shock are also observed. The molecular jet is a key component of the system, only present at the very early stages, and prominent not only in SiO and SO but also occasionally in H_2CO. The cavity walls show tracers of UV-irradiation such as hydrocarbons C_2H and c-C_3H_2 as well as CN. The hot inner envelope, apart from showing emission from complex organic molecules (COMs), also presents compact emission from small molecules like H_2S, SO, OCS and $H^{13}CN$, most likely related to ice sublimation and high-temperature chemistry. Sub-arcsecond millimeter-wave observations allow to identify those (simple) molecules that best trace each of the physical components of a protostellar system. COMs are found both in the hot inner envelope (high excitation lines) and in the outflows (lower-excitation lines) with comparable abundances. COMs can coexist with hydrocarbons in the same protostellar sources, but their origin is different. In near future, mid-IR observations with JWST–MIRI will provide complementary information about the hottest gas and the ice mantle content, at unprecedented sensitivity and at resolutions comparable to ALMA for the same sources.

5.1 Introduction

The formation of Sun-like stars is set in motion by the collapse of a cold, dense cloud. Many different physical processes take place in the protostellar stage – first few 10^5 yrs that are critical to the subsequent evolution of the star and its planetary system (Lada 1987). The mass of the star and that of its circumstellar disk are determined during this embedded phase (Hueso & Guillot 2005) and the first steps of planet formation must take place then (Greaves & Rice 2010; Williams 2012; ALMA Partnership et al. 2015; Manara et al. 2018; Harsono et al. 2018; Tobin et al. 2020; Tychoniec et al. 2018b; Tychoniec et al. 2020; Segura-Cox et al. 2020). At the same time, on larger scales, the collapsing envelope is dispersed by the energetic action of bipolar jets and winds emanating from the star-disk system which create outflows of entrained gas and dust.

Until recently, studies of low-mass protostars have suffered from low spatial resolution to disentangle these different physical components. The combination of the low temperatures (< 300 K) and high visual extinction (A_V >100) shifts the radiative processes in protostellar systems to peak in the far-infrared and submillimeter regimes. The longer the wavelength, the larger apertures are required to provide high-resolution observations. In previous lower-resolution observations, continuum emission has been readily detected, but tracing mostly the centrally-concentrated envelope, unable to disentangle the embedded disk (Hogerheijde et al. 1998; Shirley et al. 2000; Chandler & Richer 2000; Enoch et al. 2009; van Kempen et al. 2009b). Rotational transitions of molecules are a powerful tool to probe other components of the system and can be used to infer densities, temperatures, UV fields, chemical abundances and kinematics (van Dishoeck & Blake 1998; Evans 1999), but existing data often lacked sensitivity.

The advent of submillimeter interferometry opened the possibility to study protostellar systems at much smaller scales than with single-dish observations. Observations of star-forming regions with first interferometric arrays such as the Very Large Array (VLA) (e.g., Jackson et al. 1988), Owens Valley Radio Observatory (OVRO) (e.g., Chandler & Carlstrom 1996; Langer et al. 1996; Hogerheijde et al. 1999), IRAM-Plateau de Bure (IRAM-PdBI) (e.g Schilke et al. 1992; Wilner et al. 2000; Bottinelli et al. 2004), Submillimeter Array (SMA (e.g., Jørgensen et al. 2005, 2009) and others, mapped the continuum and molecular emission at few arcsecond scales, disentangling different pieces of the physical structure of the protostellar systems.

With the Atacama Large Millimeter/submillimeter Array (ALMA), it is possible to image many lines on the relevant physical scales with achievable observing times at sub-arcsecond resolution. Impressive ALMA studies of individual low-mass protostars have been presented, focusing both on simple species (< 6 atoms) and complex molecules (> 6 atoms) (e.g., Sakai et al. 2014a; Jørgensen et al. 2016; López-Sepulcre et al. 2017; Lee et al. 2019a; Codella et al. 2018; Lee et al. 2019b; Manigand et al. 2020; van Gelder et al. 2020; Bianchi et al. 2020), but larger comparative studies are still lacking. Here we present ALMA data of 16 protostellar sources covering rotational transitions of various molecules; we use these data to build a complete picture of what types of molecules trace which physical structures in protostars.

This work presents ALMA 12m-array observations of 16 protostellar sources, 10 Class 0 and 6 Class I protostars, on scales of the Solar System, ~100 au. For 5 Class 0 and 1 Class I sources, observations on protostellar envelope scales of ~2000 au are provided with the 7m Atacama Compact Array (ACA).

Class 0 sources are defined by their strong excess of submillimeter luminosity and very low bolometric temperatures <70 K (André et al. 1993; Chen et al. 1995). These sources

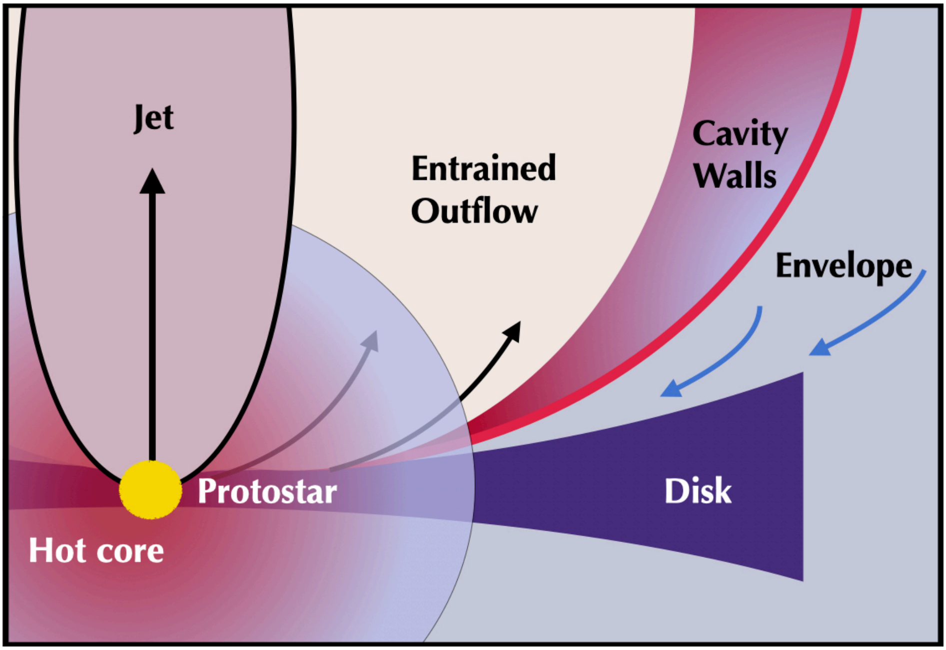

Figure 5.1: Cartoon illustrating the physical components of a protostellar system. Arrows indicate the direction of material in motion; the protostellar jet emerges from the innermost region of the protostellar-disk system. The size of the envelope with respect to the disk can vary depending on the disk size and temperature profile of the system.

are associated with powerful outflows, and the envelope mass dominates the mass of the entire system. Class I sources are defined by having an infrared spectral index indicating strong reddening (Lada 1987) with bolometric temperatures of 70–650 K (Chen et al. 1995). Those systems have already converted most of their envelope mass into disk and protostar (Crapsi et al. 2008; van Kempen et al. 2009b; Maury et al. 2011). For the typical envelope masses of sources presented here and average disk masses found by Tychoniec et al. (2020), the $M_{\rm disk}/M_{\rm env} \simeq 1\%$ for Class 0 and $\simeq 20\%$ for Class I, with values up to 75–98% in cases of rotationally supported disks (Jørgensen et al. 2009).

The targeted protostars are well-known objects located in different star-forming regions. They span a range of properties within the low-mass regime; the probed range of $L_{\rm bol}$, $T_{\rm bol}$ and $M_{\rm env}$ is presented in Fig. 5.2; those properties are provided by a suite of observations across the infrared and submillimeter spectrum (McMullin et al. 1994; Davis et al. 1999; Enoch et al. 2009; Dionatos et al. 2010; Kristensen et al. 2012; Maury et al. 2019).

Many of our sources are included in upcoming *James Webb Space Telescope* (JWST) observations with the Mid-Infrared Instrument (MIRI) (Wright et al. 2015). MIRI will provide unprecedented resolution and sensitivity in the mid-infrared (mid–IR) (5–28 μm) regime. Such mid-IR data at 0.2–0.7″ resolution will unveil the origin of the hot gas in outflows and cavity walls, as well as inner disk emission (if not too extincted) and outer envelope ice-mantle content in absorption spectra. A major limitation of MIRI is its spectral resolving power ($\lambda/\Delta\lambda \sim 3000$; $\Delta v \sim 100$ km s^{-1}) which does not reveal kinematic information of the processes in protostellar systems. MIRI is also not able to penetrate the most highly extincted

Table 5.1: Targeted protostellar systems

Source name	R.A. (J2000)	Decl. (J2000)	d (pc)	Class	L_{bol} ($L_\odot$)	T_{bol} (K)	M_{env} ($M_\odot$)	Ref.
Serpens SMM1	18:29:49.8	+01:15:20.5	439	0	109	39	58	(1)
Serpens S68N	18:29:48.1	+01:16:43.3	439	0	6	58	10	(2)
Ser-emb 8 (N)	18:29:48.7	+01:16:55.5	439	0	—	—	—	—
Serpens SMM3	18:29:59.2	+01:14:00.3	439	0	28	38	13	(1)
BHR 71	12:01:36.3	-65:08:53.0	200	0	15	44	2.7	(1)
IRAS 4B	03:29:12.0	+31 13 08.1	293	0	7	28	4.7	(1)
Per-emb-25	03:26:37.5	+30:15:27.8	293	0/I	1.9	61	2.0	(2)
B1-c	03:33:17.9	+31:09:31.8	293	0	5	48	15	(2)
HH211-mm	03:43:56.8	+32:00:50.2	293	0	2.8	27	19	(2)
L1448-mm	03:25:38.9	+30:44:05.3	293	0	13	47	15	(2)
L1527 IRS	04:39:53.9	+26:03:09.5	140	0/I	1.6	79	0.12	(3)
B5-IRS1	03:47:41.6	+32:51:43.7	293	I	7	181	3.5	(2)
TMC1	04:41:12.7	+25:46:34.8	140	I	0.9	101	0.14	(1)
IRAS 04302	04:33:16.5	+22:53:20.4	140	I	0.7	300	0.05	(1)
L1489 IRS	04:04:43.0	+26:18:57.0	140	I	3.8	200	0.2	(1)
TMC1A	04:39:34.9	+25:41:45.0	140	I	2.7	118	0.2	(1)

(1) Kristensen et al. 2012, (2) Enoch et al. 2009, (3) Green et al. 2013

inner envelope regions of Class 0 sources. This is why ALMA and JWST data are highly complementary. ALMA observes at comparable spatial resolution, but with spectral resolution at <1 km s^{-1}. ALMA also images colder gas and dust with emission lines and continuum radiation.

This work presents one of the largest combinations of high-resolution ALMA observations of Class 0/I protostars to date at three different ALMA frequency bands. Covering a broad range of protostellar properties within the low-mass regime, the aim is to identify and describe key molecular tracers of future Sun-like stars and what physical components of star-forming sources they correspond to. This work is organized as follows. In Section 2, the observations used in this work are presented, Sections 3–6 discuss molecular tracers of each of the physical components presented in Fig. 5.1. The focus is on a qualitative description, rather than quantitative analyses for which source specific models and more rotational transitions of a given molecule would be needed. Section 7 discusses various new insights from our work on the Class 0/I protostars. We summarize our work in Section 8.

5.2 Physical components of a protostellar system

The different components of protostellar systems vary significantly in their physical conditions, such as density and temperature, molecular enrichment, and dynamics. We divide the protostellar system in key physical components that are illustrated in Fig. 5.1. Our current knowledge about them is described briefly below to set the scene for the interpretation of our data.

Envelope. The envelope surrounding a protostar is the material that fuels the accretion process onto the star and disk. The physical conditions in the outer envelope on scales of a few 1000 au are reminiscent of those of starless cores with heavy freeze-out, and their chemical composition is directly inherited from the cloud out of which the star is being born (Caselli & Ceccarelli 2012). Systematic motions such as infall or expansion can occur but otherwise they are characterized by low turbulence and narrow (FWHM < 0.5 - 1 km s^{-1}) line profiles indicative of quiescent gas (Jørgensen et al. 2002).

Observations with sub-arcsecond interferometers are challenging because most of the envelope material is resolved out at high resolution. Single-dish studies have been very useful in probing the entirety of the envelope emission and pointing to the importance of molecular tracers and line ratios in understanding the physics on large scales ($\sim 10^4$ au) (e.g., Blake et al. 1994; van Dishoeck et al. 1995; Ceccarelli et al. 2000; Jørgensen et al. 2002; Maret et al. 2004; Jørgensen et al. 2004b; Sakai et al. 2008; Emprechtinger et al. 2009; Carney et al. 2016; Higuchi et al. 2018; Murillo et al. 2018). Additionally, interferometric studies at few arcsecond resolution can characterize the envelope, without losing much information on large-scale emission (e.g., Brinch et al. 2007; Chen et al. 2007; Jørgensen et al. 2007, 2009; Tobin et al. 2011, 2013).

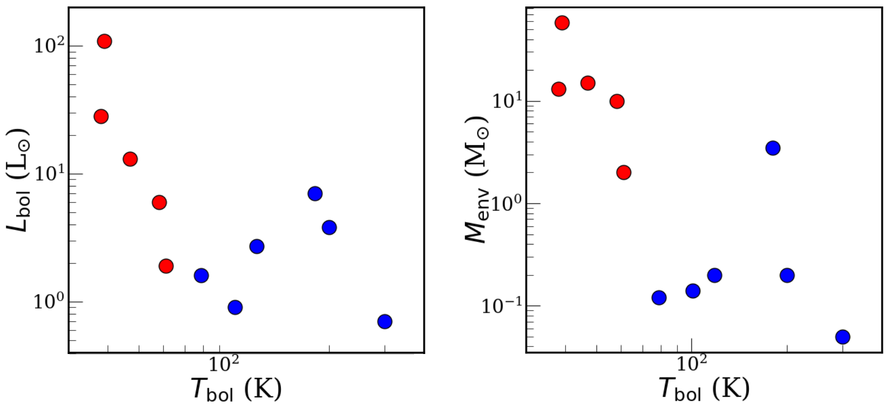

Figure 5.2: Key properties of the targeted protostars. Class 0 protostars are showed in red and Class I protostars in blue. The figures show bolometric luminosity (left) and envelope mass (right) versus bolometric temperature of protostars. The values are provided in Table 5.1 with references.

Warm inner envelope. In the innermost part of the envelope on scales of the disk, temperatures rise above 100 K, so any water and complex organic molecules (COMs) contained in ices are released from the grains back into the gas where they are readily observed at submillimeter wavelengths. This region with its unique chemical richness is called the hot core, or to distinguish it from its high-mass counterpart, hot corino (Herbst & van Dishoeck 2009).

Jets and outflows. As the material is accreting from the envelope onto the disk and protostar, excess angular momentum is released by means of collimated high-velocity jets which originate from the innermost star-disk interface regions of the protostellar system. In the earliest stages when the mass loss is at its peak, the densities are high enough to form molecules in the internal shocks in the jet (Bachiller & Gomez-Gonzalez 1992; Tafalla et al. 2010). The composition of the jet undergoes significant chemical evolution throughout the protostellar lifetime, with the molecular component being most prominent in the early stages (Nisini et al. 2015). Much slower (<20 km s^{-1}) and less collimated gas moving away from the protostar is called an outflow. It consists mostly of envelope material entrained by the jet and any wide-angle wind launched from the disk (Bjerkeli et al. 2016). Temperatures in shocked regions are much higher than in the surrounding envelope, up to a few thousand K, and sputtering of grain cores and ice mantles can further result in unique chemical signatures like SiO and other molecules (e.g., Arce et al. 2008).

Outflow cavity walls. These are the narrow zones in between the cold dense quiescent envelope material and the lower-density warm cone where outflows are propagating at large velocities. Cavity walls are exposed to UV radiation from the accreting star-disk boundary layer, which can escape through the outflow cavity without being extincted (Spaans et al. 1995). This creates conditions similar to those found in Photon Dominated Regions (PDRs), which occur throughout the interstellar medium near sources of intense UV radiation (Hollenbach & Tielens 1997). In units of the interstellar radiation field (ISRF, Draine 1978), typical values of 10^2–10^3 are found on scales of $\sim$ 1000 au (van Kempen et al. 2009a; Yıldız et al. 2012; Benz et al. 2016; Karska et al. 2018).

Young disk. In the inner envelope, a protoplanetary disk starts to form as the natural outcome of a rotating collapsing core (Ulrich 1976; Cassen & Moosman 1981; Terebey et al. 1984). A young disk should be rotating in Keplerian motion. At early stages it is difficult to identify whether the so-called embedded disk is rotationally supported, since any molecular emission from the disk is entangled with that from the envelope. In recent years several embedded disks have been identified to have Keplerian rotational structure on scales of ~100 au (Tobin et al. 2012; Murillo et al. 2013; Ohashi et al. 2014; Codella et al. 2014; Yen et al. 2017). Molecular tracers in young disks, apart from providing the kinematic information, can probe their temperature structure as well (van 't Hoff et al. 2018b). Hydrodynamical models of disk formation also predict an accretion shock as envelope material falls onto the disk (Neufeld & Hollenbach 1994; Li et al. 2011) . Some molecules, notably SO and SO_2, are proposed as tracers of such shocks (Yen et al. 2014; Sakai et al. 2014b, 2017; Artur de la Villarmois et al. 2019).

5.3 Observations

5.3.1 Datasets

Six different ALMA 12m datasets at Band 3, 5, and 6 are used in this work to cover 14 out of 16 sources. The spatial resolution of all ALMA 12m datasets is comparable (0.″3–0.″6), except for 2017.1.01174.S, where Band 3 observations are obtained at 3″. Additionally for 6 out of 16 sources in Band 6, ACA observations with 7m antennas were obtained at 6″resolution. The combined data provide a representative survey of low-mass protostars. While it does not provide a uniform observational setting for all protostars, our study presents an overview of different molecular tracers at a range of crucial spatial scales: sub-arcsecond (0.″3–0.″6) datasets provide the necessary resolution to disentangle protostellar envelope and disk component; supplemented ACA observations at 6″allow to include larger scales and inform about the components that could be resolved out by high-resolution observations.

The observations presented here are collected across several ALMA projects, and are summarized in Table 5.4. The spatial resolution allows to observe protostellar systems at solar-system scales; Band 5 and 6 observations provide a resolution of ~0.″5, which corresponds to a 70–220 au diameter for sources in our sample. Thus, regions down to 35-110 au radius in the inner envelope are probed. The Band 3 data achieve moderate resolution of ~3″which provides information on intermediate envelope scales of 500–1500 au. The ACA observations of six sources at 6″ resolution probe envelope scales of 800–2000 au. The datasets were pipeline calibrated and not self-calibrated except for 2013.1.00726.S and 2016.1.00710.S; calibrator sources and details are presented in Table 5.4.

The 2017.1.01350.S dataset (PI: Ł. Tychoniec) targets the SMM3 and TMC1 protostars in

Band 6 (1.3 mm) with ALMA 12m antennas at 0.″4 resolution, covering 13 spectral windows. Additionally for SMM3, TMC1, IRAS 4B, BHR71, Per-emb-25, and B1-c, ACA observations with 7m dishes were obtained in Band 6 at 6″with the same spectral settings as the 12m observations. The 2017.1.01174.S dataset (PI: E. van Dishoeck) targeted B1-c and S68N in Band 3 (3 mm) with ALMA 12m at 3″and B1-c, S68N, and SMM3 in Band 6 (1.3 mm) with ALMA 12m at 0.4″resolution.

The 2017.1.013781.S dataset (PI: M. van 't Hoff) targeted L448-mm, B1-c, B5-IRS1, and HH211 in Band 5 (2 mm) with ALMA 12m antennas at 0.″4 resolution. The 2017.1.01413.S dataset (PI: M. van 't Hoff) targeted IRAS-04302, L1527, L1489, TMC1, and TMC1A in Band 6 (1.3 mm) with ALMA 12m at 0.″3 resolution. The images created from all the datasets mentioned above are the result of an automated pipeline CLEAN algorithm run with automasking with the CASA software (McMullin et al. 2007). The version of CASA used for each specific dataset is specified in Table 5.4.

The 2013.1.00726.S dataset (PI: C. Hull) targets SMM1, S68N, and Ser-Emb8N in Band 6 with 0.″3 resolution in Band 6 (1.3 mm) with ALMA 12m antennas. The images presented from this dataset were produced with a manual CLEAN algorithm, with a single mask covering the entire outflow. See Hull et al. (2016); Tychoniec et al. (2019) for calibration and CLEAN algorithm details. For the same sources, Band 3 (3 mm) images were generated with manual CLEAN (dataset 2016.1.00710.S; PI: C. Hull).

5.3.2 Spectral setup of the observations

A collection of different datasets using different ALMA Bands implies varying spectral and spatial resolution as well as spectral coverage across the analysis. This is the reason that throughout this paper the sources shown in the figures differ when presenting detections and maps of different molecules. In all cases, when the molecule is discussed, only those sources where the given transition has been targeted are discussed. All non-detections are explicitly stated. Table 5.5 provides a list of targeted molecular transitions, with sources that have a particular line covered and detected or not detected.

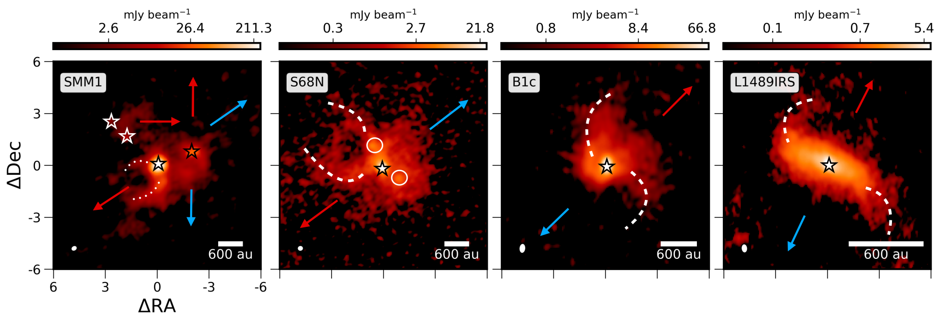

Figure 5.3: Continuum emission at 1.3 mm of four example protostellar systems obtained with ALMA at 0.″5 resolution. Symbols of stars point to confirmed protostellar sources, circles show condensations of continuum emission, without confirmed protostellar nature, dotted lines show outflow cavity walls, and dashed lines show streams of envelope material. Arrows indicate outflow directions.

The ALMA observations presented here target different spectral setups across Band 3, 5, and 6. Observations of protostellar systems require a variety of tracers to probe the strongly varying physical scales and conditions. In particular, Band 3 grants access to lines at very low excitation that enable tracing more extended material. Dust is less optically thick in Band 3 compared with Band 6 which potentially allows to peek inside the densest inner regions.

Cold outer envelopes with temperatures < 20 K are probed with low E_{up} transitions. Additionally, non-thermal processes such as sputtering of material from the grains in the outflow, will also be seen in low E_{up} due to their lower critical densities. On the other hand, thermal desorption from grains in the innermost regions are best probed with lines with high E_{up}. With the large span of frequencies of the observations, different transitions of the same molecule can be detected and used to trace different components of the system (e.g., a HNCO line at E_{up} at 15 K is available in Band 3 and lines at 70 and 125 K are covered in Band 6).

5.4 Protostellar envelope

In this section, we present molecules that trace the bulk of the protostellar envelope, which has a typical radius on the order of a few 1000 au (Jørgensen et al. 2002; Kristensen et al. 2012). Thus, the sub-arcsecond ALMA 12m array observations tend to resolve-out the envelope emission (Jørgensen et al. 2004a). For instance, the maximum recoverable scale (MRS) of ALMA Band 6 observations at 0.″4 presented here is 5″, which is between 600−2000 au diameter depending on distance to the source. For that reason, we discuss in this section mainly the ALMA-ACA observations obtained at lower spatial resolution (6″; 750−2500 au) for six sources in our datasets; Class 0 sources: B1-c, BHR71, Per-emb-25, SMM3, and IRAS 4B, and Class I source TMC1. The ACA can zoom-in on what was previously contained in a single-dish beam of 15−20″, while the MRS of ACA (30″) enables us to preserve sensitivity to large-scale emission. The MRS of all observations presented here are reported in Table 5.4.

5.4.1 Continuum emission from protostars

Figure 5.3 presents continuum emission maps toward four example protostars obtained with ALMA at ~ 0.″5. The examples illustrate most characteristic features observed in the continuum maps. The continuum images for all sources are presented in Fig. 5.17.

The continuum emission observed at millimeter wavelengths (1.3 - 3 mm in our observations) traces thermal dust emission from the inner envelope and the embedded disk. In Class 0 sources the central continuum peak is usually unresolved, showing that the embedded disk is typically compact with R_{disk} <100 au (e.g., B1-c, Fig. 5.3). The example of SMM3 (Fig. 5.17) shows a large resolved dust structure perpendicular to the outflow, but its classification as a disk is not certain. The fact that we do not observe large Class 0 disks is consistent with observations (e.g., Tobin et al. 2018; Maury et al. 2019; Tobin et al. 2020) and predictions of analytical models (Visser et al. 2009; Visser & Dullemond 2010; Harsono et al. 2015b; Machida et al. 2016).

The extended emission in Class 0 sources indicates that there is a significant amount of envelope material surrounding the protostar. In the case of the SMM1 system, presented in Fig. 5.3 (left), the continuum clumps outside the central emission are components of multiple protostellar systems, marked with stars, confirmed by the presence of individual molecular outflows (Hull et al. 2016, 2017). Binary components are also seen in TMC1 and IRAS 4B (Fig. 5.17). In the case of S68N presented in Fig. 5.3, two emission peaks that stand out of the diffuse envelope emission are marked with circles, but their protostellar nature is not confirmed.

Cavity walls are pronounced in several sources indicating a young age of these objects where the molecular jets are freshly escaping through the envelope pushing its contents to the cavity walls, see Fig. 5.3 for the case of SMM1 (dotted line). Similar structures can be seen for Emb8N, HH211 and SMM3 (Fig.5.17). In S68N, B1-c, and L1489 IRS, dashed lines highlight streamers of envelope material infalling onto the protostar, commonly observed in continuum and line observations of young systems (Alves et al. 2020; Hull et al. 2020) (Fig. 5.3).

In more evolved Class I sources, the continuum emission is dominated by the disk; there are examples of a large, resolved disk (L1489 IRS, Fig. 5.3), while others are more compact (e.g., TMC1, TMC1A, Fig. 5.17). Keplerian rotation, which can be observed only through observations of molecular gas, has so far been confirmed in L1527, TMC1, IRAS-04302, L1489 and TMC1A (Tobin et al. 2012; Harsono et al. 2014).

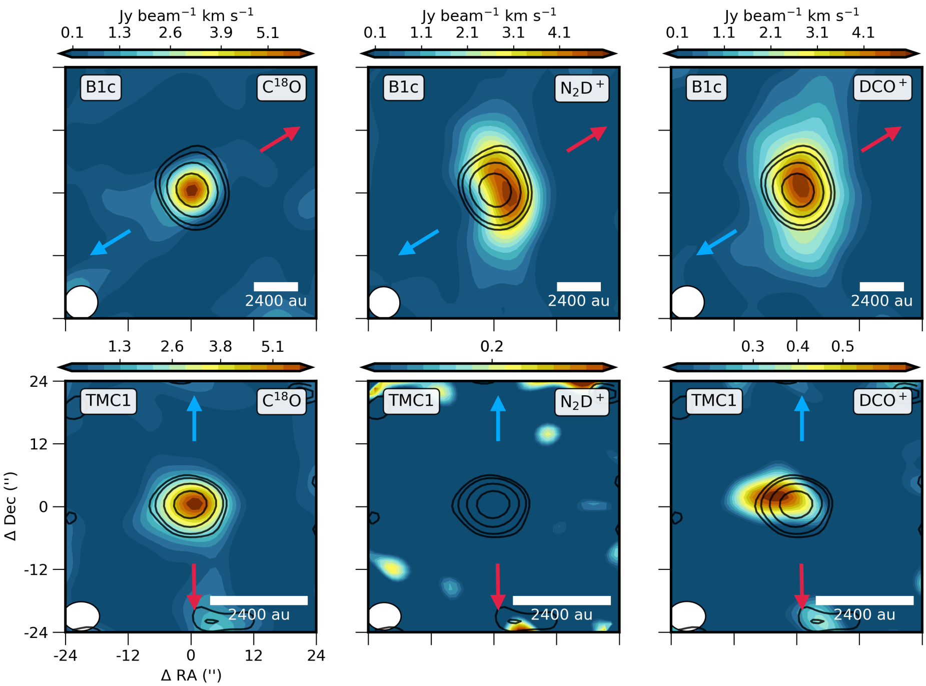

Figure 5.4: Maps of key envelope tracers toward B1-c (Class 0, top) and TMC1 (Class I, bottom) obtained with ACA. Contours represent continuum emission at 1.3 mm observed with ACA. Note different distances to B1-c and TMC1 resulting in different spatial resolutions of the maps. *Left:* $C^{18}O$ 2 − 1 *Middle:* N_2D^+ 3 − 2. *Right:* DCO^+ 3 − 2. All moment 0 maps are integrated from -2.5 to 2.5 km s^{-1} w.r.t v_{sys}.

5.4.2 Molecular lines

$C^{18}O$

In Fig. 5.4 typical envelope tracers $C^{18}O$ 2–1 (E_{up} = 16 K), DCO^+ 3–2 (E_{up} = 21 K), and N_2D^+ 3–2 (E_{up} = 22 K), observed at 6″resolution with the ACA, are presented toward example Class 0 and Class I sources – B1-c and TMC1, respectively. The emission from the presented molecules exhibits similar behaviour for all Class 0 sources, therefore B1-c serves as a representative case; TMC1 is the only Class I source in the sample with 7m observations available. The maps for all sources for which these molecules have been targeted can be found in Appendix A.2. All envelope tracers presented here are characterized by narrow line profiles with FWHM ~ 1 km s^{-1}.

The $C^{18}O$ emission peak coincides with the continuum peak for our six sources and appears to be compact, less than 1000 au diameter for B1-c and TMC1. For B1-c and all Class 0 sources (Fig. 5.18), low-level extended $C^{18}O$ emission is seen along the outflow direction. For the only Class I source targeted with the ACA, emission is marginally resolved in the direction perpendicular to the outflow.

$C^{18}O$ is a good tracer of high column density material, however, it becomes less abundant as soon as the dust temperature drops below the CO freeze-out temperature (~ 20–25 K). There is also a density threshold: CO freeze-out only occurs at densities above ~ 10^4–10^5 cm^{-3}, because at lower densities the timescales for freeze-out are longer than the lifetime of the core (Caselli et al. 1999; Jørgensen et al. 2005).

For 4 out of 6 sources presented at 6″resolution, Kristensen et al. (2012) performed modeling of the SED and sub-mm spatial extent using the DUSTY code (Ivezic & Elitzur 1997). The results provide, among other properties, a temperature structure throughout the envelope and the radius at which the temperature drops below 10 K, which is considered as the border between envelope and the parent cloud. Kristensen et al. (2012) obtained radii of 3800, 5000, 6700, and 9900 au for IRAS4B, TMC1, SMM3, and BHR71, respectively. The compact $C^{18}O$ emission observed on-source and its non-detection over the full expected extent of the protostellar envelope can be explained by CO freeze-out occurring already within the inner 1800 – 2500 au radius, which is the spatial resolution of our observations for Class 0 sources. This upper limit on the CO snowline is consistent with CO snowlines typically observed and modeled toward other Class 0 protostars (Jørgensen et al. 2004b; Anderl et al. 2016; Hsieh et al. 2019b).

Equation 1 from Frimann et al. (2017) allows to calculate the expected CO snow line for the current luminosity of the example sources B1-c and TMC1 presented in Fig. 5.4 in the absence of an outburst. For B1-c the snowline is expected to be at 200–400 au radius depending on the assumptions of the sublimation temperature (smaller radii for 21 K and larger for 28 K), while the TMC1 CO snowline is expected to be at 100–200 au. For the most luminous source with $C^{18}O$ 7m observations available, the expected radius is at 400–750 au. Therefore clearly in all cases the expected CO snowline is well within the 7m beam.

In high-resolution studies, the CO emission is often seen at greater distances than expected from the current luminosities of those protostars. This is attributed to accretion bursts of material which increase their luminosities resulting in a shift of the observed CO emission radius up to a few times its expected value (but usually still within a 1000 au radius) (Jørgensen et al. 2015; Frimann et al. 2017; Hsieh et al. 2019b). Therefore, we cannot say anything about past accretion burst based on these data.

N_2D^+ and DCO^+

In our observations N_2D^+ is seen extended in the direction perpendicular to the core rotation axis, which is typically the same as the outflow rotation axis, toward B1-c (Fig. 5.4) and other Class 0 sources except IRAS 4B (Fig.5.19). In the case of IRAS 4B the emission from this molecule appears dominated by large-scale emission from the filament detected toward this source, connecting it with IRAS 4A (Sakai et al. 2012). The peak of the N_2D^+ emission is significantly shifted from the continuum peak in all cases, with a significant decrease in the inner regions in some cases (see BHR 71 in Fig. 5.19). Similar extended N_2D^+ emission in other Class 0 sources was seen by Tobin et al. (2013) based on lower resolution OVRO data. For TMC1 the N_2D^+ molecule is not detected.

The DCO^+ emission is seen extended in a similar fashion to what is observed for N_2D^+. However, contrary to N_2D^+, DCO^+ is brightest on the continuum peak for all sources except TMC1 and Per-emb-25. For these two sources, the emission peak is offset by 1000–2000 au from the continuum source in the direction perpendicular to the outflow.

Both DCO^+ and N_2D^+ are considered cold gas tracers. N_2D^+ is efficiently destroyed by CO in the gas-phase, therefore freeze-out of CO results in N_2D^+ being retained in the gas-phase at larger radii of the envelope, where temperatures are lower. This behaviour has been demonstrated in several other protostellar sources by Tobin et al. (2011, 2013).

Both DCO^+ and N_2D^+ are produced through reactions with H_2D^+. At cold temperatures the H_2D^+ abundance is enhanced through the H_3^+ + HD → H_2D^+ + H_2 reaction, which is exothermic by 230 K. As the reverse reaction is endothermic, low temperatures increase H_2D^+. Additionally, both H_3^+ and H_2D^+ are enhanced in gas where CO has been depleted. However, the CO molecule is still needed for the production of DCO^+ through the H_2D^+ + CO reaction. Therefore, DCO^+ is expected to be most abundant around the CO snowline (Jørgensen et al. 2004b; Mathews et al. 2013). Warmer production routes through CH_2D^+ + CO are also possible (Wootten 1987; Favre et al. 2015; Carney et al. 2018).

The difference between DCO^+ and N_2D^+ chemistry is reflected in the morphology of the emission observed toward our sample. As DCO^+ requires gas-phase CO for its formation, it peaks close to the CO snowline, which is within the resolution of our observations (~1800–2500 au radius), while N_2D^+ is only located where CO is not present in the gas phase. Therefore we observe a significant decrease of N_2D^+ in the inner envelope. If the warm production of DCO^+ is triggered in the inner regions, this will additionally produce DCO^+ within the beam of our observations, hence DCO^+ does not decrease in the inner envelope. The extent of the DCO^+ and N_2D^+ emission in each source is comparable, ranging from ~ 5000 au in B1-c and BHR71 to 1500 au in TMC1, suggesting that their outside radii trace the region where CO becomes present again in the gas phase due to the low density.

The morphology of the emission from cold gas tracers such as DCO^+ and N_2D^+ is sensitive to the density and temperature profile of the system, which can be affected by system geometry (i.e., outflow opening angle, disk flaring angle, flattening of the envelope). DCO^+ has been shown to increase its abundance in the cold shadows of a large embedded disk (Murillo et al. 2015).

In the Class I source, DCO^+ is present on much smaller scales (< 2000 au radius) than in Class 0 sources and no N_2D+ is seen. Emission from those molecules is consistent with a picture of a dissipating envelope in Class I sources, resulting in less dense, warmer gas surrounding the protostar. TMC1 has an order of magnitude lower envelope mass compared to the Class 0 sources (Table 5.1; Kristensen et al. 2012). This causes the extent of the cold and dense region to shrink, preventing N_2D^+ from being detected, and limiting the extent of DCO^+ emission. The dense gas toward TMC1 is clearly present only in the flattened structure surrounding the binary system, likely forming a young, embedded disk. In fact this source is suggested to have a rotationally-supported circumbinary disk (Harsono et al. 2014; van't Hoff et al. 2020). The geometry of the disk can create favourable conditions for the DCO^+ enhancement in the cold shadows of the disk.

Other relevant molecules that trace the quiescent envelope material but are not presented here are HCO^+ and $H^{13}CO^+$ (Hogerheijde et al. 1997; Jørgensen et al. 2007; Hsieh et al. 2019b, van 't Hoff et al. in prep.). These molecules have been shown to probe the material outside of the water snowline (Jørgensen et al. 2013; van 't Hoff et al. 2018a). As water sublimates at temperatures $\sim$ 100 K, much higher than CO, HCO^+ can be seen throughout the envelope, except for the warmest inner regions. N_2H^+ is tracing the envelope material and CO snowline and has been shown to peak closer to the central protostar than N_2D^+ (Tobin et al. 2013). Their ratio can potentially be used as an evolutionary tracer of protostars (Emprechtinger et al. 2009).

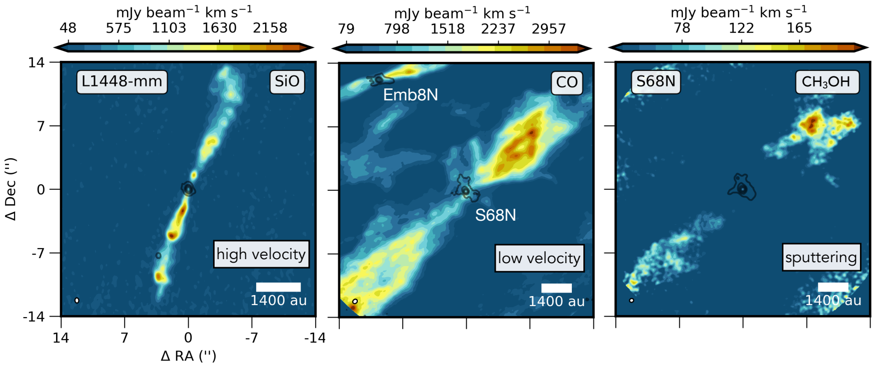

Figure 5.5: Maps of three different components of the outflow. Moment 0 maps are presented in color scale with continuum emission at 1.3 mm in black contours, both obtained with ALMA 12m observations. *Left:* An extremely high-velocity (EHV) molecular jet illustrated with the SiO (4–3) map for L1448-mm integrated from -70 to -50 and from 50 to 70 km s^{-1} w.r.t υ_{sys}. *Middle:* Low-velocity outflow illustrated with the CO 2–1 map for S68N integrated from -15 to -3 and from 3 to 15 km s^{-1} w.r.t υ_{sys}. *Right:* Ice mantle content released with shock sputtering presented with the CH_3OH ($2_{1,0}$ – $1_{0,0}$) map for S68N integrated from -8 to -1 and from 1 to 8 km s^{-1} w.r.t υ_{sys}. The CO outflow from Ser-emb-8N is present at the edge of the map.

In summary, the quiescent envelope material is traced by dense and/or cold gas tracers. Chemical interactions result in N_2D^+ tracing the outer envelope where CO is frozen-out, whereas DCO^+ is seen both in the outer envelope as well as in the inner regions, tracing the unresolved CO snowline. $C^{18}O$ is a good tracer of dense (n > 10^5 cm^{-3}) and warm (T > 30 K) regions in the inner 2000 au radius of the protostellar systems. The protostellar evolution from Class 0 to Class I is evident as the envelope becomes less dense and more warm and the protostellar luminosity can heat up dust and gas more easily.

5.5 Outflows and jets

Outflowing material from protostellar systems is best analyzed with kinematic information. In the following section, we will discuss three different components of protostellar outflows observed with the ALMA 12m array: 1) the high-velocity jet (>30 km s^{-1}), 2) the low-velocity entrained outflow (<30 km s^{-1}), 3) the gas that results from the interaction with the outflow – ice sputtering products at velocities close to that of ambient material, but with linewidths significantly broader (up to 15 km s^{-1}) than the quiescent envelope tracers. The three components are presented in Fig. 5.5 with examples of S68N, a representative case of a prominent outflow and ice sputtering, and L1448-mm, a source with a prototypical high-velocity jet.

5.5.1 Extremely high-velocity jet

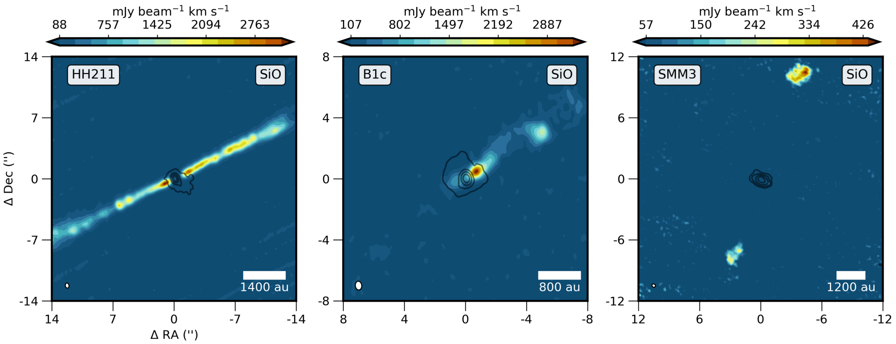

Figure 5.6: Maps of the EHV jets observed in SiO. Moment 0 maps are presented in color scale with continuum emission at 1.3 mm presented in black contours, both obtained with 12m observations. SiO 4–3 map of HH211 integrated from -20 to -10 and from 10 to 20 km s^{-1} w.r.t v_{sys}; B1-c ntegrated from -70 to -40 and from 40 to 70 km s^{-1} w.r.t v_{sys}; SMM3 integrated from -60 to -40 and from 20 to 35 km s^{-1} w.r.t v_{sys}.

Figure 5.6 presents the extremely high-velocity (EHV) molecular jet component for HH211, B1c, and SMM3 observed in SiO with the ALMA 12m array; the L1448-mm EHV is shown in Fig. 5.5. The latter and HH211 are well-known EHV sources (Guilloteau et al. 1992; Lee et al. 2007) while SMM3 and B1-c are new detections of the jet component. HH211 shows SiO emission at low-velocities because the outflow is almost in the plane of the sky, but the high velocities are evident from the large proper motion movements of the bullets (~115 km s^{-1}; Lee et al. 2015). CO, H_2CO, and SiO in the EHV jets of Emb8N and SMM1 are presented in detail in Hull et al. (2016) and Tychoniec et al. (2019). Altogether, these detections in 6 out of 7 Class 0 sources targeted at high-resolution, strengthen the conclusion that EHV jets are more common than previously thought in Class 0 sources.

In the case of L1448-mm and HH211, there are several molecular bullets along the jet axis with velocities up to 100 km s^{-1}, while both B1c and SMM3 show a much simpler structure with two bullets detected on one side in the former and a single pair of symmetrically placed bullets observed in the latter case. B1-c actually has a pair of bullets ~ 200 au from the continuum peak, with the other bullet at 2500 au only seen in the redshifted part of the jet. The emission in SiO and SO appears very similar (Fig. 5.22, Fig. 5.23). There are no other molecules tracing the high-velocity component toward this source. H_2CO and ^{12}CO are not targeted with our ALMA 12m datasets toward B1-c. The SMM3 jet has two distinct high-velocity bullets at ~ 3200 au from the source which appear similar in CO, SiO and SO (see

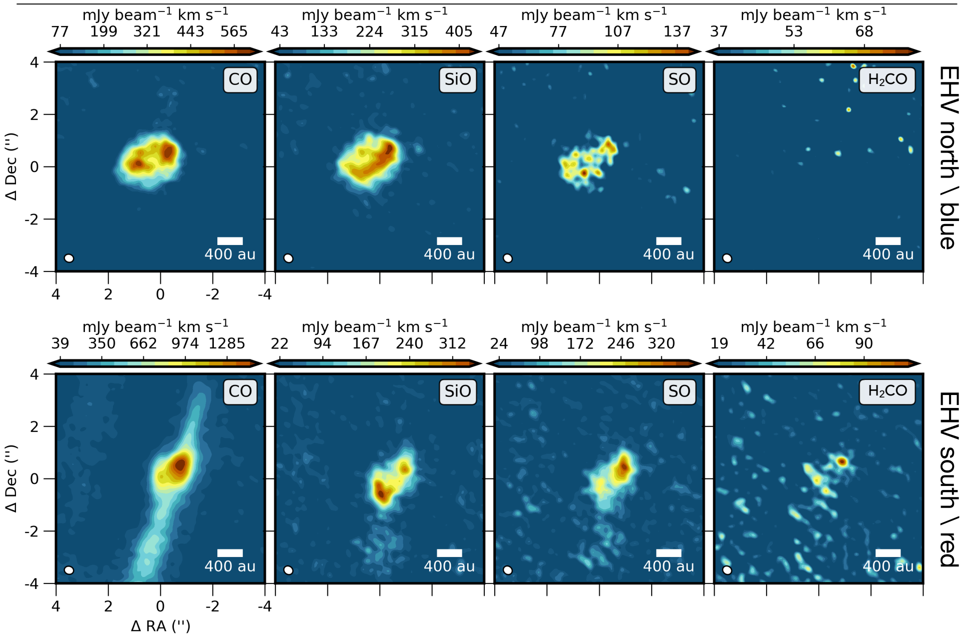

Figure 5.7: Zoom-in on molecular bullets from the SMM3 jet (see Fig. 5.6). CO, SiO, SO, and H_2CO molecular transitions are presented. *Top:* Norther/blueshifted bullet. Moment 0 maps are integrated from -60 to -40 km s^{-1} w.r.t v_{sys}. The map center is offset from the SMM3 continuum center by (−3″.7, +10″.3). *Bottom:* Southern/redshifted bullet. Moment 0 maps are integrated from 20 to 40 km s^{-1}. The map center is offset from the SMM3 continuum center by (+2″.7, −7″.).

zoom-in on Fig 5.7). Additionally, the redshifted bullet shows faint, but significant emission from H_2CO. No traces of H_2CO are found in the blueshifted outflow.

These data are particularly interesting as still only few molecules tracing EHV jets have been identified to date (see Lee 2020 for review). Apart from those presented here – CO, SiO, SO, and H_2CO– molecules such as HCO^+ and H_2O have been seen in this high-velocity component (Kristensen et al. 2012; Lee et al. 2014). What is especially important to highlight is the third detection of a H_2CO bullet in SMM3 after IRAS04166 (Tafalla et al. 2010) and Emb8N (Tychoniec et al. 2019). This detection means that either a significant fraction of ice-coated dust is released with the jet, or that the H_2CO is efficiently produced in the jet through gas-phase chemistry.

It is argued that the molecular jet tracers have a very different physical origin than the protostellar outflows. Contrary to the low-velocity outflow, which consists mostly of entrained envelope material, the EHV jet is expected to be directly launched from the innermost region of the system (Tafalla et al. 2010; Lee 2020). The high-velocity jet is comprised of atomic material which readily forms molecules in the high-density clumps (internal working surfaces; Raga et al. 1990; Santiago-García et al. 2009) that are resulting from shocks in the jet, which are produced by the velocity variations of the ejection. This in turn means that by observing the high-velocity bullets, one gains insight on the variability of the accretion process (Raga et al. 1990; Stone & Norman 1993). The new EHV sources B1c and SMM3 show bullet spacings of 1200 au in B1c and 3200 au in SMM3, which can be converted using the terminal velocity of the jets (not corrected for inclination) to the dynamical ages of 80 and

250 years, respectively. If the central mass of the protostar can be estimated this can be used to provide the orbital period of the component causing the variability (Lee 2020).

The fact that the EHV jet tracers are dominated by O-bearing molecules has been associated with a low C/O ratio in the jet material (Tafalla et al. 2010). For high mass-loss rates, molecules are produced efficiently in the jet from the launched atomic material (Glassgold et al. 1991; Raga et al. 2005; Tabone et al. 2020). Additionally the ratio of SiO-to-CO can indicate the presence of dust in the launched material, which can in turn inform about the jet launching radius, i.e., whether it is inside or outside the dust sublimation radius (Tabone et al. 2020). The new detections of high-velocity jets suggest that this process may be occurring in every young Class 0 object. Studying large samples of objects with ALMA and combining with multi-transition observations can unveil the atomic abundances of the inner regions, which are difficult to measure otherwise directly (McClure 2019).

In summary: O-bearing species such as CO, SiO, SO, and H_2CO observed at high velocities are excellent tracers of the chemistry within the protostellar jet. Those molecules most likely formed in the internal working surfaces from the material carried away from the launching region of the jet.

5.5.2 Low-velocity outflow

Figure 5.8 presents low-velocity outflow tracers CO 2–1 ($E_{\rm up}$ = 16 K) for TMC1, SO 5_6–4_5 ($E_{\rm up}$ = 35 K), and SiO 4–3 ($E_{\rm up}$ = 21 K) for B1c. In Fig. 5.21 we present an overview of CO 2–1 emission for five sources obtained with the ALMA 12 m array at $0\farcs4$ resolution. The sources show a variety of emission structures in the low velocity gas (<20 km s^{-1}). In all cases, we do not capture the entirety of the outflows as they extend beyond the primary beam of observations (~ 30″). SMM3 and Emb8N have very narrow outflow opening angles (< 20 degrees), while SMM1, S68N and TMC1 present larger opening angles.

CO emission is especially prominent in the cavity walls, which can be related to both the limb brightening effect as well as higher (column) density of the material in the outflow cavity walls. This is especially highlighted in the Class I source, TMC1, where CO emission is almost exclusively seen in the outflow cavity walls. Even though CO is piling up in this region, it is observed at velocities up to 15 km s^{-1} so it is clearly tracing the entrained material and not the quiescent envelope. The lower envelope density in Class I results in less material to be entrained in the outflow. In SMM1, three CO outflows from SMM1-a, SMM1-b, and SMM1-d are overlapping (Hull et al. 2016; Tychoniec et al. 2019).

The CO molecule traces the bulk of the gas as it is the most abundant molecule detectable in the sub-mm regime. It serves as an indicator of the outflow extent and gas morphology, as it is not affected by chemical processing in shocks. It can also be used to quantify the total mass-loss rates, using the dense cloud abundance ratio of CO/H_2 ~ 10^{-4}. A well-known correlation between molecular outflows and protostellar luminosities indicates a strong link between the accretion and ejection processes (Cabrit & Bertout 1992; Bontemps et al. 1996; Mottram et al. 2017). The decrease in accretion and total envelope mass with evolution of the system also results in fainter, less powerful outflows. The weak emission from the Class I source TMC1, which is an order of magnitude lower in intensity with respect to outflows from Class 0 protostars, is consistent with this trend.

In Fig. 5.22, SiO maps are presented: Band 5 SiO 4–3 ($E_{\rm up}$ = 21 K) and Band 6 SiO 5–4 ($E_{\rm up}$ = 31 K) data are shown in velocity ranges corresponding to the low-velocity outflow. In contrast to CO emission, the low-velocity SiO is mostly observed in clumps of emission instead of tracing the entirety of the outflowing gas. Several such clumps can be seen in the S68N source. In some cases, the clumps are relatively symmetric (Emb8N, B1-c), while monopolar emission is seen in other examples (L1448-mm, SMM1-d). In the case of SMM1-a and SMM1-b, very weak SiO emission at low velocities is observed. SiO emission in outflows is exclusively present in the Class 0 sources, while absent in the Class I sources, TMC1 and B5-IRS1, covered in these data sets.

SiO is a molecule that is enhanced by several orders of magnitude in shocks compared with gas in cold and dense clouds where most of the Si is locked in the grains (e.g., Guilloteau et al. 1992; Dutrey et al. 1997). Shocks release Si atoms from the grains by means of sputtering and grain destruction, leading to subsequent reactions with OH, another product of shocks, forming SiO (Caselli et al. 1997; Schilke et al. 1997; Gusdorf et al. 2008b,a). Thus, SiO is much more prominent in high-velocity gas, where grains are more efficiently destroyed (see Section 4.1), than in low-velocity shocks.

SO is a shock tracer, similarly to SiO. Fig. 5.23 presents SO 5_6–4_5 ($E_{\rm up}$ = 35 K) and SO 6_7–5_6 ($E_{\rm up}$ = 47 K) observations in Band 6. The emitting regions of SO are comparable with those of SiO for the Class 0 sources. The cases of S68N and B1-c show that SO emission also peaks at the source position while SiO is absent there. Thus, SO and SiO do not always follow each other and some SO might be associated with hot core emission (Drozdovskaya et al. 2018). Important differences are observed for TMC1, where SO seems to be associated with the remainder of the envelope or the disk, while the SiO is not detected toward this source, as mentioned above.

SO is enhanced in shocks through reactions of atomic S released from the grains with OH, as well as through H_2S converted to SO with atomic oxygen and OH (Hartquist et al. 1980; Millar & Williams 1993). Shocks could also explain the emission toward TMC1, where weak accretion shocks onto the disk could enhance the SO abundances (Sakai et al. 2014b; Yen et al. 2014; Podio et al. 2015). Overall, there is a clear decrease of both SiO and SO low-velocity emission from Class 0 to Class I. Either the less powerful jet cannot destroy the grains and create conditions for the production of SiO and SO and/or the much less dense envelope and outflow cavity walls do not provide enough dust grains for creating large column densities of those molecules; additionally, the excitation conditions might change significantly with evolution of the protostellar system, hampering the detection of even low-J SO and SiO transitions with critical densities in the 10^5 – 10^6 cm^{-3} range.

HCN 1–0 ($E_{\rm up}$ = 4 K) and H^{13}CN 2–1 ($E_{\rm up}$ = 12 K) maps are presented in Fig. 5.24 and 5.25, respectively. HCN is clearly seen in outflowing material enhanced in similar regions as low-velocity SiO. For Emb8N the HCN emission has been associated with intermediate velocity shock (Tychoniec et al. 2019). In B1-c and L1448-mm weak extended emission along the outflow direction is detected but H^{13}CN strongly peaks on source. In the case of HH211, H^{13}CN is seen only in the outflow, with a geometry consistent with the outflow cavity walls, but with velocity profiles that are consistent with the outflowing material.

HCN is associated with the most energetic outflows (Jørgensen et al. 2004; Walker-Smith et al. 2014) and is enhanced at high temperatures in shocks. H^{13}CN is likely associated with both the hot inner regions (not detected in HCN due to optical thickness of the line) and the low-velocity outflow (Tychoniec et al. 2019; Yang et al. 2020). The geometry of H^{13}CN emission seen in HH211 resembles a cavity wall: it could be a result of CN produced by UV-photodissociation and subsequent production of HCN via the H_2 + CN reaction, which requires high temperatures (Bruderer et al. 2009; Visser et al. 2018). The fact that H^{13}CN is seen at outflow velocities shows that shocks are required to produce HCN, which is likely released at the cavity walls and then dragged with the outflow.

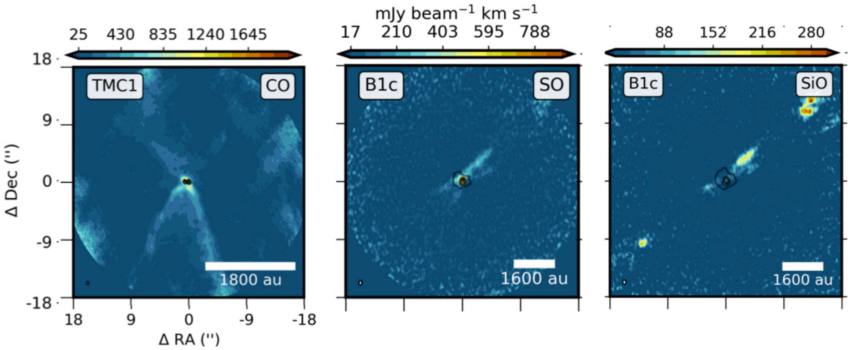

Figure 5.8: Low-velocity outflow in CO, SO, and SiO. Moment 0 maps of CO toward TMC1, SO and SiO map toward B1c are integrated from -10 to 10 km s^{-1} w.r.t v_{sys}.

5.5.3 Shock sputtering products

Ice-mantle tracers are a different class of molecules detected in low-velocity protostellar outflows. They are produced and entrained through interactions between the jet and the envelope. Here we present ALMA 12m array observations in Band 6 at 0″.5 resolution for CO 2 − 1 ($E_{\rm up}$ = 17 K), CH_3OH $2_{1,0} - 1_{0,0}$ ($E_{\rm up}$ = 28 K), and H_2CO $3_{0,3} - 2_{0,2}$ ($E_{\rm up}$ = 21 K) , and in Band 3 at 3″ for CH_3CN $6_1 - 5_1$ ($E_{\rm up}$ = 26 K), CH_3CHO $6_{1,6,0} - 5_{1,5,0}$ ($E_{\rm up}$ = 21 K), and HNCO $5_{0,5} - 5_{0,4}$ ($E_{\rm up}$ = 16 K). Fig. 5.9 compares maps of integrated emission from those molecules with those of CO for S68N. All ice-mantle tracers detected in the outflow are observed in their low-energy transitions.

The shape of the emission of these ice-mantle tracers is somewhat similar. CH_3CN and HNCO are clearly brighter on the redshifted part of the outflow (south-east) and CH_3CHO are brighter in the blueshifted (north-west) side. CH_3OH and H_2CO show an even distribution between the two lobes. The peak intensity for all species occurs at significant distances from the source (~ 5000 au) and in some cases the emission drops below the detection limit closer to the source. This is contrary to the CO emission, which can be traced all the way back to the central source. In all tracers the emission is also detected at the continuum position, however, this emission has a narrow profile and results from thermal sublimation of ices in the hot core of S68N (van Gelder et al. 2020).

The velocities observed for ice-mantle tracers in the outflow are <15 km s^{-1} with respect to the systemic velocity. This is slower than the CO and SiO outflow line wings which have velocities up to 20–30 km s^{-1}. On the other hand, the lines are clearly broader than those of molecular tracers of UV-irradiated regions that trace passively heated gas (see Section 5). The velocities observed for CH_3OH and other ice-mantle tracers are high enough for these molecules to be material near the outflow cavity walls, where ice mantles could be sputtered. These molecules therefore most likely trace low-velocity entrained material with a considerable population of ice-coated grains that are sputtered in the shock (Tielens et al. 1994; Buckle & Fuller 2002; Arce et al. 2008; Jiménez-Serra et al. 2008; Burkhardt et al. 2016). Thermal desorption of molecules from grains is not likely as dust temperatures are below 100 K in the outflow cavity walls at distances of few times 10^3 au for low-mass stars, and at those temperatures most COMs are frozen out on grains. The fact that there is no enhancement of these tracers closer to the source also argues against emission being related to high temperature.

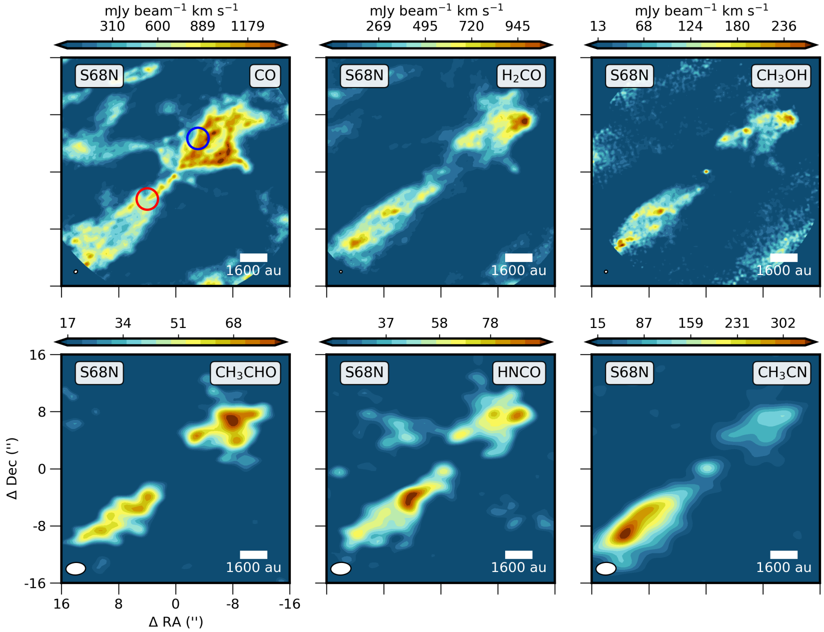

Figure 5.9: Maps of the ice mantle tracers toward the S68N outflow, with the CO low-velocity outflow map for reference. *Top:* CO, H_2CO and CH_3OH moment 0 maps obtained in Band 6 at 0.″5 resolution. Circles show regions from which spectra were obtained for analysis in Section 7.1. *Bottom:* CH_3CHO, HNCO, and CH_3CN moment 0 maps obtained in Band 3 at 2.″5 resolution. The emission is integrated from -10 to -1 km s^{-1} and from 1 to 10 km s^{-1} w.r.t υ_{sys}.

The prototypical outflow source with complex organic chemistry – the L1157-B1 shock spot – exhibits emission from many species. Complex molecules such as CH_3OCHO and C_2H_5OH (Arce et al. 2008), H_2CCO, $HCOCH_2OH$, CH_3OCH_3 (Lefloch et al. 2017) and NH_2CHO (Codella et al. 2017) are seen. The abundances of some COMs w.r.t. CH_3OH detected at the B1 position exceed those of 'hot corinos' by a factor of 2 to 10. However, the largest molecules seen in warm inner envelopes of protostars are not detected at L1157-B1 (Lefloch et al. 2017). THe hot core and outflow chemical composition for source S68N are compared in Section 7.1.

The complex structure of H_2CO seen in S68N at low-velocities contrasts with the simple kinematic structure of the high-velocity bullet seen in SMM3 (Section 4.1, Fig. 5.7). The origin of the H_2CO emission for these two sources could be different, with the low-velocity emission arising from the sputtering of ices, whereas the presence of H_2CO in the jet could result from gas-phase production through the reaction of CH_3 with O. Alternatively, if the icy grains were launched with the jet, they could be sputtered in the internal working surfaces at high velocities (Tychoniec et al. 2019).

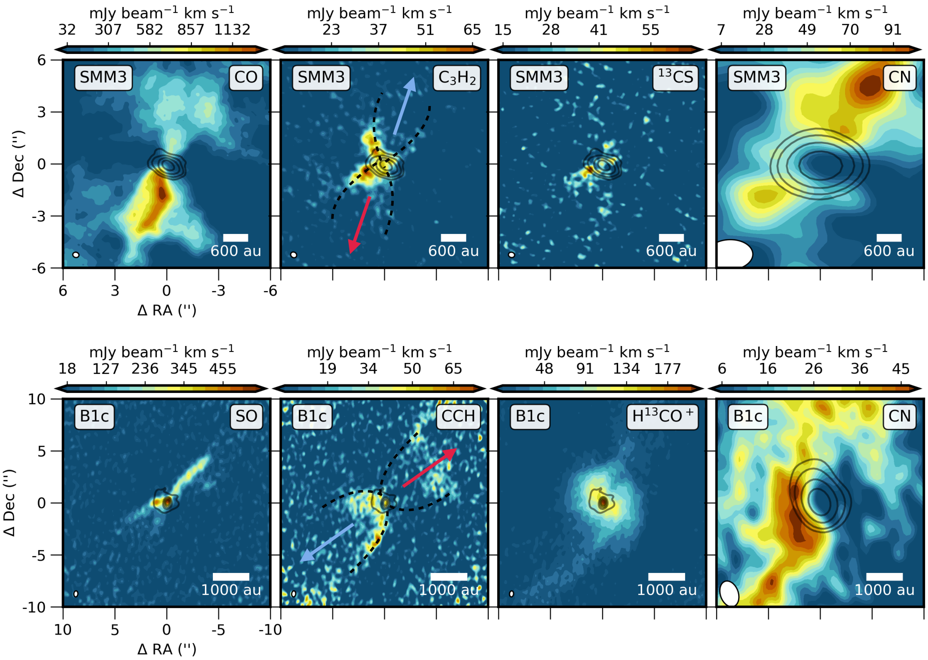

Figure 5.10: Maps of the outflow cavity wall tracers toward SMM3 and B1c, with low-velocity outflow map for reference. *Top:* Moment 0 maps toward SMM3 of CO 2–1, c-C_3H_2 $6_{1,6}$–$5_{0,5}$, and ^{13}CS 5–4 obtained in Band 6 at 0.″5 resolution and CN 1–0 in Band 3 at 3″. *Bottom:* Moment 0 maps toward B1c of SO 6_7–5_6, C_2H $3_{2.5,3}$–$2_{1.5,1}$ and $H^{13}CO^+$ 3–2 obtained at 0.″5 and CN 1–0 at 3″. The emission is integrated from -5 to -1 km s^{-1} and from 1 to 5 km s^{-1} w.r.t v_{lsr}. Outflow directions and delineated cavity walls are showed in C_2H and C_3H_2 maps.

5.6 Outflow cavity walls

In this section, we highlight key molecules detected in the outflow cavity walls. It is challenging to precisely distinguish cavity walls from the outflowing material. The velocity of the gas in the cavity walls should be lower than in the outflow, as the cavity wall contains envelope material at rest but which is passively heated by UV radiation. We first discuss maps of species associated with cavity walls and then their line profiles.

5.6.1 Maps

Figure 5.10 presents integrated emission maps of key tracers discussed in this section for two examples: SMM3 and B1-c. Plots for the remainder sources (S68N, Emb8N, and TMC1) are presented in the Appendix in Fig. 5.26.

Key tracers of the outflow cavity walls are simple unsaturated hydrocarbon molecules: c-C_3H_2 $4_{4,1}$–$3_{3,0}$ ($E_{\rm up}$ = 32 K) for SMM3 and TMC1, and C_2H $3_{2.5,3}$–$2_{1.5,2}$ ($E_{\rm up}$ = 25 K) for S68N, B1-c, and Emb8N, as seen in maps obtained with ALMA Band 6 at 0.″5 resolution.

In Emb8N and SMM3 the emission from C_2H and c-C_3H_2, respectively, is symmetric; it appears similar in extent and shape on both sides of the continuum source. Comparison with CO emission, which traces the bulk of the outflowing gas, indicates that the hydrocarbons are located in the outflow cavity walls close to the source. For B1-c, the emission from C_2H is U-shaped suggestive of a cavity wall, stronger on the blueshifted side of the outflow, which could be either a projection effect or an asymmetry in the envelope structure. For B1-c no ALMA CO observations exist to compare with the bulk of the outflow at comparable resolution; however, the other outflow tracer, SO, confirms the outflow direction and rough extent of the outflow cavity walls. Moreover, the shape of the cavity walls is consistent with the appearance of the CO 3–2 outflow observed with SMA toward this source at 4″resolution (Stephens et al. 2018).

S68N presents a chaotic structure (Fig. 5.26, top), but C_2H is found elongated in the outflow direction. While it is difficult to identify the cavity wall, the C_2H emission surrounds the CO outflow emission. The C_2H emission toward this source is asymmetric, with stronger emission in the blueshifted part of the outflow. Emission of c-C_3H_2 toward the Class I source TMC1 (Fig. 5.26, bottom) is not directly related to the cavity walls, but is extended perpendicular to the outflow, which suggests that c-C_3H_2 traces the envelope or extended disk material.

Both c-C_3H_2 and C_2H have been prominently observed in PDRs such as the Horsehead Nebula and the Orion Bar tracing the layers of the cloud where UV-radiation photodissociates molecules, which helps to maintain high atomic carbon abundance in the gas-phase that is needed to build these molecules. C_2H is enhanced in the presence of UV radiation at cloud densities (Fuente et al. 1993; Hogerheijde et al. 1995) and c-C_3H_2 usually shows a good correlation with C_2H (Teyssier et al. 2004). Both molecules have efficient formation routes involving C and C^+, although models with only PDR chemistry tend to underpredict their abundances, especially for c-C_3H_2. A proposed additional mechanism is the top-down destruction of PAHs (Teyssier et al. 2004; Pety et al. 2005, 2012; Guzmán et al. 2015); the spatial coincidence of PAH emission bands with hydrocarbons in PDRs is consistent with that interpretation (van der Wiel et al. 2009).

It is instructive to compare the conditions between classic PDRs and outflow cavity walls around low-mass protostars.The G_0 value for Orion Bar is estimated at 2.6×10^4 (Marconi et al. 1998), while the Horsehead Nebula has a much more moderate field of 10^2 (Abergel et al. 2003). The UV radiation field around low-mass protostars measured by various tracers is 10^2–10^3 at ~ 1000 au from the protostar (Benz et al. 2016; Yıldız et al. 2015; Karska et al. 2018), therefore the PDR origin of small hydrocarbons is plausible. The top-down production of hydrocarbons due to PAHs destruction does not appear to be an efficient route here, as PAHs are not commonly observed in low-mass protostellar systems (Geers et al. 2009), and the UV-fields required for this process are above 10^3 (Abergel et al. 2003).

The difference in morphology of hydrocarbons between Class 0 and Class I systems – outflow cavity walls in Class 0 versus rotating disk-like structure in Class I – is most likely related to the evolution of the protostellar systems. Class 0 sources have a dense envelope and the UV radiation can only penetrate the exposed outflow cavity walls, while for Class I it is likely much easier for both the UV radiation from the accreting protostar and the interstellar radiation to reach deeper into the envelope or disk.

Figure 5.10 also shows CN 1–0 ($E_{\rm up}$ = 5 K) observed at 3″resolution in Band 3 for SMM3 and B1-c. Compared with C_2H, CN is tracing similar regions. In S68N CN has a similar extent as C_2H but not over the full extent of the outflow traced by CO. In B1-c, the CN emission has a similar shape of the cavity wall cone as seen in C_2H, but also a significant contribution from larger scales is detected. In all cases the CN emission avoids the central region, which likely results from on-source absorption by the foreground CN molecules.

TMC1 presents a high-resolution example of CN emission (Fig. 5.26). The offset between

CO and CN reveals a physical structure of the inner regions of the protostellar system: the entrained outflow traced with CO appears closer to the jet axis, while CN highlights the border between the outflow cavity wall and quiescent envelope. CN is sensitive to UV radiation, as it can be produced with atomic C and N, whose abundances are enhanced in PDRs, with UV photodissociation of HCN contributing as well (Fuente et al. 1993; Jansen et al. 1995; Walsh et al. 2010; Visser et al. 2018).

$H^{13}CO^+$ emission is presented for B1c (Fig. 5.10) and S68N (Fig. 5.26) observed in Band 6 at 0.″4 resolution. The bulk of the emission from this molecule appears to be related to the cold envelope, however streams of material can be seen in B1-c and S68N. The streams of gas observed in $H^{13}CO^+$ are coincident with the cavity wall observed in C_2H. As $H^{13}CO^+$ is expected to probe the dense envelope, the similarity of the morphology of the traced material between $H^{13}CO^+$ and C_2H and CN shows that the envelope material is UV-irradiated. ^{13}CS observed in Band 6 with the 12m array is detected for SMM3 (Fig. 5.10). Weak emission from this molecule is observed in TMC1. The morphology of ^{13}CS emission is very similar to that of c-C_3H_2.

The ^{13}CS molecule, as a high-density tracer likely traces the material piling up on the cavity walls pushed by the outflow. This emission is usually slow (± 2 km s^{-1}) indicating that this is not outflowing gas but rather envelope material on the outflowing cavity walls.

Faint emission of ^{13}CS towards the Class I source TMC1 is consistent with the dissipating envelope as the source evolves, hence no high-density material is seen in the remnant cavity walls, even though they are still highlighted by the CO emission.

5.6.2 Spectral profiles - cavity walls or entrained outflow

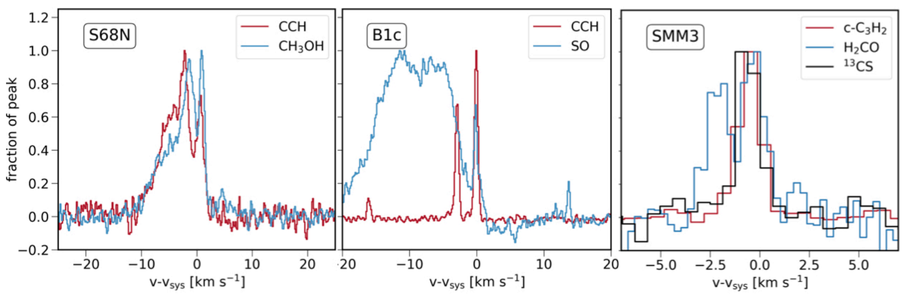

Figure 5.11: Spectra obtained at the cavity wall positions for hydrocarbons (red) and ice-mantle tracers (blue). *Left:* C_2H $3_{2.5,2}$–$2_{1.5,1}$ (E_{up} = 25 K) and CH_3OH $2_{1,0}$–$1_{0,1}$ (E_{up} = 28 K) spectra for S68N, *Middle:* C_2H $3_{2.5,2}$–$2_{1.5,1}$ (E_{up} = 25 K) and SO 6_7–5_6 (E_{up} = 48 K) spectra for B1-c, *Right:* c-C_3H_2 $4_{4,1}$–$3_{3,0}$ (E_{up} = 32 K), H_2CO $3_{2,1}$–$2_{2,0}$ (E_{up} = 68 K), and ^{13}CS 5–4 (E_{up} = 33 K) spectra for SMM3.

In Fig. 5.11 spectra of ice mantle tracers, CH_3OH and H_2CO, and the hydrocarbon molecules, C_2H and C_3H_2 are presented. All spectra are shifted by their source velocity to zero km s^{-1}. In case of S68N, it is seen that C_2H and CH_3OH have very similar line profiles indicating that they trace similar material. The width of ~ 10 km^{-1} suggests that this material is entrained with the outflow. A narrow component appears to be superposed at systemic velocities. Note that fine splitting of C_2H blends the spectra although the other transition at +2 km s^{-1} does not affect the blueshifted velocity component. In contrast, B1c shows only remarkably narrow C_2H line profiles with a FWHM of ~ 2 km s^{-1}, and SMM3 has similarly narrow c-C_3H_2 and ^{13}CS lines compared with broader H_2CO emission (Fig. 5.11, right) . This is consistent with emission from well-defined cavity walls seen toward those sources.

The case of moderate ~ 10 km s^{-1} velocity material observed toward S68N indicates that the C_2H line does not in all sources trace exclusively the quiescent cavity walls. The profile is consistent with the observed morphology of the line (see Fig. 5.26) – emission is seen up to a few thousand au from the source and its shape does not resemble a cavity wall as clearly as in other sources. The narrow component centered at systemic velocity seen in Fig. 5.11 indicates that while the broad component might be dominating the emission, the UV-irradiated cavity wall also contributes to the emission observed for S68N. S68N could be a very young source, as the chaotic structure of its outflow and envelope indicates (Le Gouellec et al. 2019). The high abundances of freshly released ice-mantle components described in Section 4.3 are consistent with this interpretation (see also Section 7.1). It is also possible that UV radiation produced locally in shocks is causing the enhancement of C_2H emission at higher velocities.

To summarize, we observe the hydrocarbons C_2H and c-C_3H_2, as well as CN, $H^{13}CO^+$ and ^{13}CS in the outflow cavity walls of Class 0 protostars. These tracers show that the outflow cavity walls are regions with enhanced density compared with the rest of the envelope exposed to the protostellar UV radiation, resulting from the interaction of the protostellar outflow with the cavity walls. Some of those molecules also likely have enhanced abundances. C_2H, as the most abundant of the hydrocarbons presented here, is also seen prominently across the envelope at velocities comparable to the low-velocity outflow whereas c-C_3H_2 appears as a clean tracer of the quiescent, UV-irradiated gas in the cavity walls in the Class 0 sources.

5.7 Inner envelope

5.7.1 Compact emission

The inner regions of young protostellar systems are characterized by high temperatures which result in a rich chemistry as molecules that form efficiently in ices on grains in cold clouds sublimate into the gas phase. Complex organic molecules (COMs) detected in these datasets are discussed quantitatively in detail elsewhere, for both O-bearing by van Gelder et al. (2020) and for N-bearing species by Nazari et al. (subm.). In this section we focus on smaller molecules that also trace the innermost hot core regions and therefore are likely abundant in ices. This includes several small S-bearing molecules.

Fig. 5.12 shows emission from H_2CCO, HNCO, t-HCOOH, SO, H_2CS, and $H^{13}CN$ for the Class 0 protostar B1-c, and H_2S and OCS lines for SMM3; all data are observed with the ALMA 12m array at 0.″5.

The SO 6_7–5_6 $E_{\rm up}$ = 48 K line is seen to peak on the central source for B1-c and S68N (Fig. 5.23). SO has already been discussed in the outflow (Section 6), but it is also prominent in the inner envelope. While the spatial resolution does not allow to disentangle the hot corino emission from the small-scale outflow on a few hundred au scale, there is a difference between these two sources and SMM3 and Emb8N. The latter two sources show a substantial decrease in SO intensity towards the continuum peak, i.e., they have prominent SO emission in the outflow, but not from the hot corino. This suggests that sources like B1-c and S68N, which are bright in SO toward the continuum emission peak, have an additional component

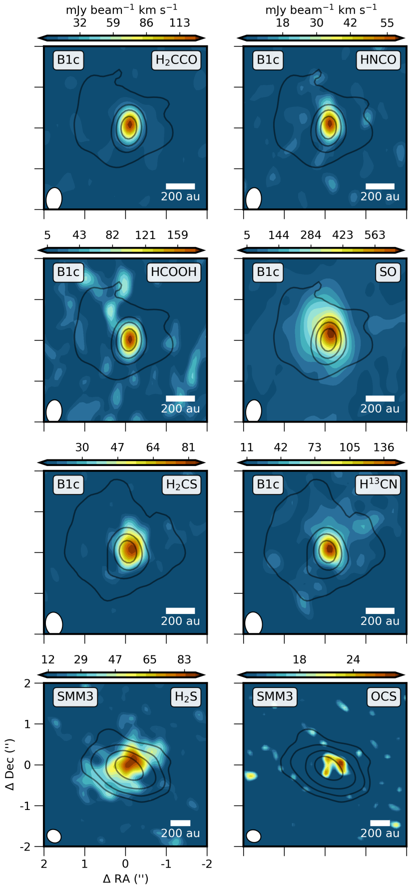

Figure 5.12: Compact emission for B1-c and SMM3 for various molecules tracing the warm inner envelope (hot corino). Moment 0 maps shown in colorscale integrated from -3 to 3 km s^{-1} w.r.t v_{sys}. 1.3 mm continuum presented in contours.

responsible for SO emission. This is highlighted by the narrower lines of SO toward the continuum peak compared with the outflow in S68N (Fig. 5.27). The narrow component, visible in spectra taken on-source, has a width of ~ 5 km s^{-1}. The main component of the spectrum taken in the blueshifted outflow has a similar width but has a more prominent line wing up to 20 km s^{-1}.

Both B1-c and S68N are sources characterized as hot corinos (Bergner et al. 2017; van Gelder et al. 2020), which means that the conditions in their inner regions are favourable for release of molecules from the ice mantles. For the well-studied case of IRAS16293-2422, Drozdovskaya et al. (2018) have also identified a hot core component of SO based on isotopologue data, in addition to an SO component in the large scale outflow. Overall, SO appears to be present in ices.

TMC1 shows SO emission clearly toward both components of the binary system, slightly offset from the central position (Fig. 5.23). There is also a molecular ridge present in SO close

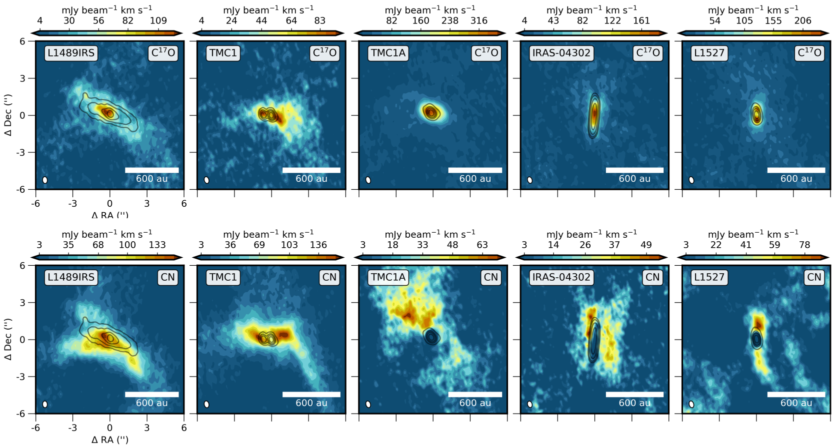

Figure 5.13: Images of Class I disks observed with ALMA 12m in Band 6 (van't Hoff et al. 2020). *Top:* Moment 0 maps of $C^{17}O$ at $0\farcs4$ resolution integrated from -10 to 10 km s^{-1} w.r.t v_{sys}. *Bottom:* Moment 0 maps of CN integrated from -2 to 2 km s^{-1} w.r.t v_{sys}. Continuum contours in black.

to the disk-envelope interface.

This morphology could be an accretion as the accretion shocks are much weaker than shocks that cause the SO emission seen in the outflows (Section 4), the SO is likely released from the icy mantles with the infalling material (Sakai et al. 2014b). Narrow linewidths of SO toward TMC1 seem to rule out the shock scenario, and is more likely associated with emission along the cavity walls (Harsono et al. 2020).

HNCO and $HN^{13}CO$ are detected toward B1-c and S68N peaking on source in higher $E_{\rm up}$ transitions (Nazari et al., subm.). For lines with $E_{\rm up}$ <90 K an extended component is also detected in the outflow. SMM3 and Emb8N have no detections of HNCO on source, but for SMM3 this molecule appears in the outflow. For all Class I sources where the relatively strong HNCO $11_{0,11}-10_{0,10}$ line (A_{ij} = 2×10^{-4} s^{-1}, $E_{\rm up}$=70 K) was targeted, it was not detected.

HNCO emission has been modeled by Hernández-Gómez et al. (2018) and suggested to be a superposition of both warm inner regions of the envelope as well as the colder, outer envelope. Its similar behaviour to sulphur-bearing species, also observed in our work, is proposed to be related to the fact that O_2 and OH are involved in formation of species like SO and HNCO (Rodríguez-Fernández et al. 2010).

OCS is detected toward SMM3 peaking in the center; S68N and SMM1 show centrally peaked $OC^{33}S$ detection, a minor isotopologue signaling a high abundance of OCS. In all cases the emission is moderately resolved; of size ~ 200 au in case of SMM3 and detected up to 500 au away from source for S68N and SMM1.

H_2S shows strong emission toward SMM3 and is also weakly present in TMC1. For SMM3 the emission is resolved along the outflow direction and perpendicular to the expected disk axis. Those are the only two sources for which H_2S 12m array data were taken. Additionally, the 7m data presented in the Appendix show prominent, centrally peaked H_2S emission for four more sources. H_2S is expected to be the dominant sulphur carrier in ices (Taquet et al. 2020). However, it has not yet been detected in ice absorption spectra to date (Boogert et al. 2015). The weak emission from H_2S in dark clouds has been modeled as a result of the photodesorption of ices at the outside of the cloud (like in the case of H_2O, Caselli et al. 2012), while chemical desorption is important for grains deeper inside the cloud but outside the water snowline (Navarro-Almaida et al. 2020). These models are consistent with H_2S ice containing most of the sulphur.

H_2CS is detected for B1-c, S68N and L1448-mm through a line with E_{up} = 38 K. Another transition with E_{up} = 46 K is found in Class I disks: IRAS-04302, L1489, and TMC1A. In B1-c, the emission is marginally resolved, while in IRAS-04302 the molecule is clearly seen across the midplane, indicating release at temperatures of at least 20 K (van't Hoff et al. 2020; Podio et al. 2020). Multiple lines of H_2CS are a powerful tool to probe the warm > 100 K, innermost regions of the protostellar systems (van 't Hoff et al. 2020).

H_2CCO is detected for B1-c and S68N. For the lower E_{up} = 100 K transition, the molecule is also detected in the outflow. For Class I sources, the transition at comparable energy is not detected. HCOOH is detected for B1-c and S68N with low-energy transitions that are seen both on source and in the outflow, while the higher energy line (E_{up} = 83 K) is seen only on source. $H^{13}CN$ is detected in B1-c and L1448-mm on source, additionally to the outflow component.

While B1-c and S68N are characterized as hot corinos with many COM lines detected (van Gelder et al. 2020), and L1448-mm has warm water in the inner regions (Codella et al. 2010), SMM3 does not appear to have significant emission from COMs. Moreover, simple molecules associated with the hot core for B1-c, such as SO and H_2CO, are only seen outside of the SMM3 central source. While it is possible that the optically thick continuum prevents a detection of COMs in its inner envelope (De Simone et al. 2020), differences in chemistry or physical structure (e.g., a large cold disk, see Section 6.2) between the SMM3 and the hot corino sources are also possible. The fact that emission from OCS and H_2S is centrally peaked (Fig. 5.12, bottom row) suggests that continuum optical depth is not an issue, although both those species could be a result of grain destruction or ices sputtering, therefore not necessarily coming from the midplane but rather from the surface of a disk-like structure.

5.7.2 Embedded disks

Disks are commonly observed in Class I sources (Harsono et al. 2014; Yen et al. 2017), as the envelope clears out. Fig. 5.13 presents maps of the $C^{17}O$ 2–1 (E_{up} = 16 K) and CN 2–1 (E_{up} =16 K) lines toward Class I disks and L1527-IRS, which is identified as a Class 0/I object, observed with ALMA 12m at 0.″3 resolution. The $C^{17}O$ and H_2CO emission for disks in Taurus using these data are analyzed in detail by van't Hoff et al. (2020). Here we discuss CN in comparison with $C^{17}O$.

$C^{17}O$ is observed concentrated towards the continuum emission for all disks, and is a much cleaner tracer of the disk than any other more abundant CO isotopologues, although even $C^{17}O$ still shows some trace emission from the surrounding envelope. In the case of large edge-on disks like IRAS-04302 and L1527, the vertical structure of the emission can be probed, as well as the radius where CO freeze-out occurs. Overall, Class I disks are warmer than their Class II counterparts with CO freeze-out taking place only in the outermost regions (Harsono et al. 2015a; van 't Hoff et al. 2018a; van't Hoff et al. 2020; Zhang et al. 2020).

We detect CN in all observed Class I disks, although it does not trace the midplane of the disk. In the near edge-on example of IRAS-04302, the CN emission originates from the upper layers of the disks, in the same direction as the outflow, which is perpendicular to the disk in this source. This opens a possibility that the emission is also related to the irradiated residual cavity walls in those sources. TMC1A is a clear example where CN is tracing the same material as probed by Bjerkeli et al. (2016) in CO, which is attributed to a disk wind. TMC1 and L1527 show CN oriented in the same direction as the disk; in TMC1 there is also a clear filament structure on larger scales irradiated by the UV from the protostar, seen also in other tracers.

In comparison with the $C^{17}O$ emission, which traces the midplane disk, CN thus appears in the upper layers and in the outflow, therefore in most cases the two molecules are mutually exclusive. This picture is consistent with the bulk density traced by CO and the irradiated layers of the disk and envelope exposed to UV traced by CN. Recent observations of a sample of Class I sources including IRAS-04302 by Garufi et al. (2020). is consistent with CN not tracing the disk.

In the younger Class 0 sources characterization of the disk is much more difficult because of the strong envelope emission. Nevertheless, several Keplerian disks have been identified with observations of CO isotopologues like $C^{18}O$ (Tobin et al. 2012; Murillo et al. 2013). Our data allow us to investigate this for the case of SMM3. Fig. 5.28 shows the red and blue-shifted emission from $C^{18}O$ toward SMM3. There is a clear rotational signature in the direction perpendicular to the outflow on scales of a few hundred au. However, to unambiguously identify the disk and its radius, higher spatial and spectral resolution data are necessary.

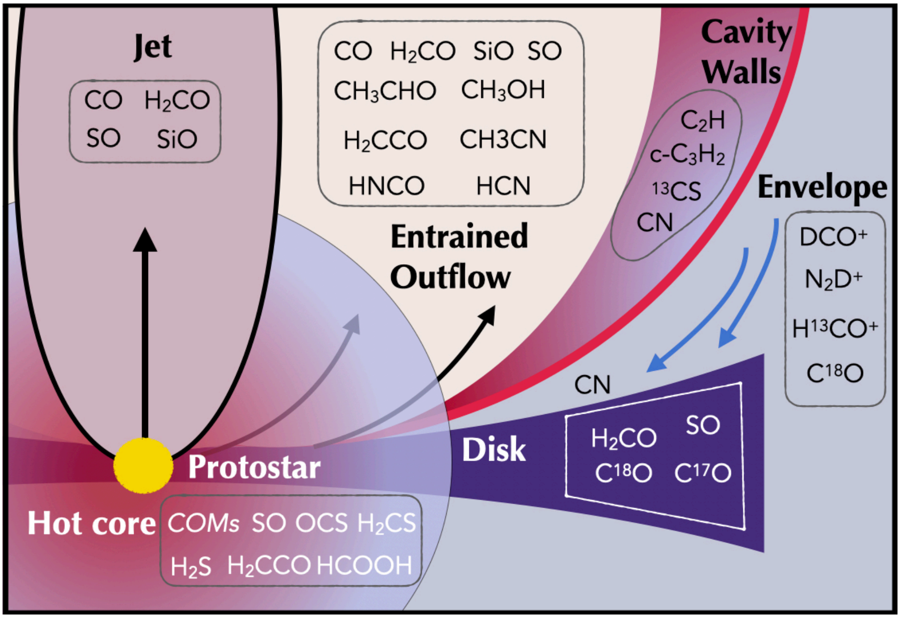

Figure 5.14: Summary cartoon of the key molecular tracers of different components, exclusive to molecules presented in this work.

5.8 Discussion

Figure 5.14 summarizes our findings about which molecule traces which component in Class 0/I protostars. Table 5.5 lists all molecules discussed in this work with indication of the physical component that they trace. Below, we will address several implications of the results.

Table 5.2: Molecular tracers of physical components

Molecule	Envelope	Disk	Hot corino	Outflow	Jet	Cavity
CO	✓	–	–	✓	✓	✓
$C^{18}O$	✓	✓	–	✓	–	✓
^{13}CO	✓	✓	–	✓	–	✓
$C^{17}O$	✓	✓	✓	–	–	✓
$H^{13}CO^+$	✓	–	–	✓	–	✓
H_2CO	✓	✓	✓	✓	✓	–
H_2CS	–	✓	✓	–	–	–
SO	–	✓	✓	✓	✓	–
SiO	–	–	–	✓	✓	–
DCO^+	✓	–	–	–	–	–
N_2D^+	✓	–	–	–	–	–
OCS	–	–	✓	–	–	–
HNCO	–	–	✓	✓	–	–
H_2CCO	–	–	✓	✓	–	–
HCOOH	–	–	✓	✓	–	–
^{13}CS	✓	–	–	–	–	✓
CN	✓	✓	–	–	–	✓
HCN	–	–	–	✓	–	–
$H^{13}CN$	–	–	✓	✓	–	–
C_2H	✓	–	–	✓	–	✓
c-C_3H_2	–	–	–	–	–	✓
CH_3CHO	–	–	✓	✓	–	–
CH_3CN	–	–	✓	✓	–	–
CH_3OCHO	–	–	✓	✓	–	–
CH_3OH	–	–	✓	✓	–	–

5.8.1 COMs in outflow versus hot core

COMs are detected already in the prestellar stage of star formation (Bacmann et al. 2012; Scibelli & Shirley 2020), where they are thought to be efficiently produced on the surfaces of the icy grains. Small amounts can subsequently be released back into the gas through various non-thermal desorption processes, and/or be re-formed by gas-phase reactions. In the inner envelope, temperatures are high enough that thermal desorption of ices is enabled. In the outflow cavity walls, sputtering by shocks can release ices from the grains. COMs in the hot core are detected through high excitation lines while COMs in the outflow are observed primarily through transitions of low $E_{\rm up}$. Therefore, comparing the observations of molecular complexity in outflows with hot cores can unveil if there is any warm temperature processing of the ices, and whether some molecules also have a gas phase production route.

We therefore calculate abundance ratios between different ice mantle species and methanol at three positions for S68N: one on source, obtained from van Gelder et al. (2020) and Nazari et al. (subm.), and one each in the blueshifted and redshifted part of the outflow. We measure the abundance of the species in a 3″region centered on CH_3OH peak on the blueshifted and redshifted region. The size of the region is based on the spatial resolution of the Band 3 data. The regions are indicated in Fig. 5.9. From these regions we obtain the average brightness temperature which are converted to column density using the same formulation as in Tychoniec et al. (2019). The emission is assumed to be optically thin, and the excitation temperature $T_{\rm ex}$ is taken to be 20 K, typical of subthermally excited molecules with large dipole moments in outflow gas.

The assumption of optically thin emission needs to be verified, especially in the case of CH_3OH which is the most abundant ice species. Since it is the reference molecule for our comparison, by underestimating the column density of methanol, the relative abundance of other molecules can be overestimated. Only a single CH_3OH line is detected in the outflow in our data set, 2_1–1_0 ($E_{\rm up}$ = 62 K). Escape probability calculations show that even at the lower densities in outflows this CH_3OH line is likely optically thick. No optically thin CH_3OH

isotopologue is detected in the outflow of S68N, therefore we provide an upper limit for the $^{13}CH_3OH$ $5_{2,3}$-$4_{1,3}$ E_{up} =56 K line. The upper limit on this $^{13}CH_3OH$ line translates to an upper limit on the CH_3OH column density that is a factor of 5 higher, assuming ^{12}C / ^{13}C = 70. Thus, our CH_3OH column densities in the outflow could be underestimated by up to a factor of 5. Methanol abundances from the hot corino of S68N reported in van Gelder et al. (2020) are corrected for optical thickness with $^{13}CH_3OH$.

Figure 5.15 compares the abundance ratios of various species with respect to methanol for S68N. First, it is seen that the relative abundances are remarkably similar on both sides of the outflow, well within the uncertainties. That could mean that sputtering is the main reason for the molecules to be released. For gas phase reactions to produce similar abundances, both the conditions and timescales need to be similar on both sides of the outflow. Second, most abundances relative to CH_3OH are found to be comparable to the hot core within our uncertainties and those of van Gelder et al. (2020) and Nazari et al. (subm.), noting that due to lack of optically thin CH_3OH line detected in the outflow, our uncertainties are much larger. The greatest difference is seen for CH_3OCHO, which could be attributed to additional gas-phase formation in the hot core, but because of the large uncertainties with the optically thick CH_3OH this is only tentative result. More transitions, especially optically thin isotopologues of CH_3OH and other complex molecules, are needed to provide a robust conclusion.

For the well-studied L1157 outflow, Codella et al. (2020) find CH_3CHO/CH_3OH is 0.5%. which they find in agreement with ratios in hot cores toward different protostars, but not including L1157 itself. In the case of S68N we uniquely show a comparison between the emission from molecules in the outflows and hot core for the same source. While modeling by Codella et al. (2020) shows that the similar spatial origin of CH_3OH and CH_3CHO does not imply that they are both solely grain sputtering products, an agreement between hot cores and outflows could mean that similar processes are responsible for emission in both regions.

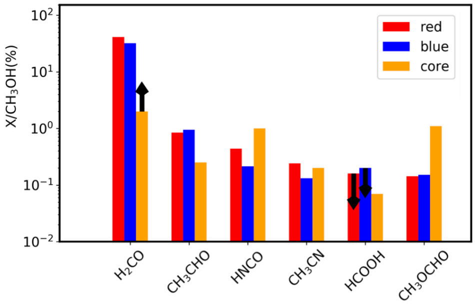

Figure 5.15: Column density ratios of molecules to CH_3OH in S68N. The ratios are shown for a 3″region in both redshifted and blueshifted part of the outflow. The central 0.″5 region with abundance ratios from (van Gelder et al. 2020, Nazari et al. subm.)

It is interesting that the SMM3 outflow shows ice mantle tracers in the outflow but not on the source. Thus, the lack of hot corino emission is likely due to the physical conditions in the inner regions such as a large disk (Section 6.2) or continuum optical depth (De Simone et al. 2020) and not to the lack of complex molecules on the grains. Since methanol is not detected, we cannot provide abundance ratios for this outflow. B1-c - another source with an outflow containing ice mantle products, has methanol lines overlapping with the high-velocity SO outflow, therefore precise abundance measurements are not possible.

JWST will be able to provide information on the ice content due to rich absorption spectra in the mid-IR. The abundances of COMs in the gas-phase provided by ALMA (van Gelder et al. 2020, Nazari et al. subm.) can then be directly compared with the ice content. So far, the ice content observed on cloud scales with *Spitzer* does not show a correlation with the gas content but those data do not probe thermally desorbed ices (Perotti et al. 2020).

5.8.2 Carbon-chains and other hydrocarbons vs COMs

Early observations at low spatial resolution suggested that large carbon-chains such as C_5H, HC_7N, and HC_9N and complex organic molecules are mutually exclusive and therefore the two were proposed to be tracers of two different categories of protostellar sources driven by different chemistry, namely warm carbon-chain chemistry (WCCC) and hot core chemistry (Sakai & Yamamoto 2013). Warm carbon-chain chemistry is thought to occur above the sublimation temperature of CH_4 ~ at 30 K. The proposed difference then lies in the WCCC sources collapsing more rapidly than the hot core sources, which prevents CO to accumulate on the ices, leaving a higher CH_4 ice content. Thus, in WCCC sources, there would be less CO to form more complex organic molecules such as CH_3OH, and an underabundance of COMs is indeed observed. This scenario has been supported by the lower deuteration observed in WCCC sources (Sakai et al. 2009). With ALMA observations at higher resolution and sensitivity, sources harboring both COMs and small hydrocarbons, c-C_3H_2 and C_2H, have now been observed (Imai et al. 2016; Oya et al. 2017).

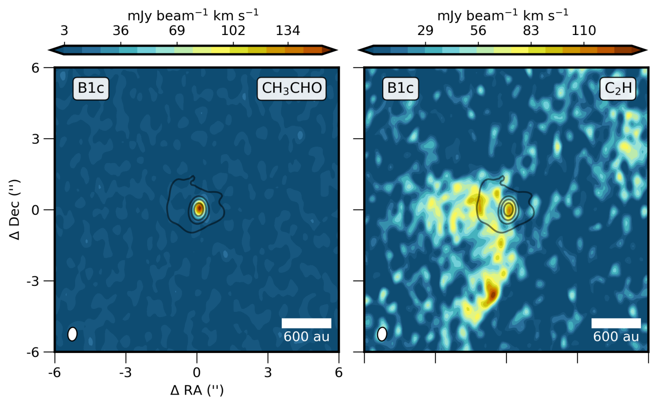

Figure 5.16: Emission maps of an example COM and hydrocarbon toward B1-c. *Left:* CH_3CHO moment 0 map, *Right:* C_2H moment 0 map; both integrated from -2 to 2 km s^{-1} w.r.t v_{sys}.

Our data also show detection of small hydrocarbons and COMs in the same sources (Fig. 5.16). However, our high resolution maps now show those hydrocarbons to originate in the UV irradiated outflow cavity walls (Section 5). Both c-C_3H_2 and C_2H can be solely explained by PDR chemistry (Guzmán et al. 2015; Cuadrado et al. 2015) even in moderate UV fields of low-mass protostars and therefore WCCC chemistry does not need to be invoked for the sources presented in this work. The PDR origin is consistent with our observed geometry at the edges of the cavities, where lower extinction allows the UV radiation from the protostellar accretion to easily reach this region. It also explains confinement of this emission to the inner 2000 au of the envelope, as the UV radiation decreases with distance from the source.

Table 5.3: Summary of evolution of chemical tracers

Component	Class 0	Class I
Envelope	Cold, dense envelope results in cold tracers (DCO^+, N_2H^+)	Envelope dissipates, extent of cold tracers is much smaller
Jet	O-bearing molecules (CO, SiO, SO, H_2CO) are present in high-velocity bullets	Molecular jet disappears, seen only in atomic and ionised gas
Outflow	Ice sputtering (CH_3OH, HNCO) and grain destruction (SO, SiO) tracers are present	Decreased outflow mass and less dense envelope result in no tracers of sputtering and grain destruction, only faint CO remains
Cavity walls	Prominent signs of UV-irradiated cavity walls (CN, C_2H, c-C_3H_2)	No prominent signs of hydrocarbons in cavity walls, CN still present
Hot corino	COMs and simple tracers of ice sublimation and high-temperature chemistry (H_2S, OCS)	Small extent plus disk shadowing results in less complexity, except for outbursting sources
Disk	Warm disk with COMs, dust obscuration	Colder disk molecules, Keplerian rotation seen in H_2CO, $C^{18}O$, CN in the disk surface.

A deep search for larger hydrocarbons like HC_5N in cavity walls could help to understand their origin.

5.8.3 Class 0 vs Class I in different components

There are many processes that take place within the protostellar lifetime of a few 10^5 yr that alter the chemical composition and physical conditions. First, the envelope is dissipating and the radius where key molecules are in the gas-phase is becoming smaller (Jørgensen et al. 2005). With high resolution studies it is possible to now probe different snowlines in unprecedented detail (van 't Hoff et al. 2018a; Hsieh et al. 2019b). There is a clear evolutionary trend observed in temperature – Class 0 disks are generally warmer than Class II disks, with Class I sources in between, which has major impact on the richness of their spectra (van 't Hoff et al. 2020; van't Hoff et al. 2020).

Molecular EHV jets are only present in the Class 0 phase (Nisini et al. 2015) whereas the lower velocity outflows in these stages are rich in ice mantle tracers. The Class I jets are invisible in molecular tracers and their outflows only show primarily CO, with much less contribution from shock tracers such as SO and SiO.

Complex organic molecules are a key tracer of chemistry at early stages. We see them in the outflows only in Class 0 sources. This is likely due to the decrease of the outflow force and mass and envelope density. In the inner regions, the physical conditions such as temperature and density also favour the early stages for the abundances of COMs. In rare cases of rich chemistry in Class I disks, it is usually attributed to accretion outbursts heating up the disk (van 't Hoff et al. 2018c; Lee et al. 2019a).

Cavity walls are seen prominently in the Class 0 sources in molecules whose abundances are sensitive to UV radiation. In Class I sources a flared disk and weak outflow remain. While there is less envelope to attenuate the UV radiation, there is also less material to irradiate, which results in less prominent emission from UV tracers on large scales in Class I. Another example of a transition of molecular appearance between Class 0 and I is SO: this molecule traces primarily the outflow in Class 0 and the disk-envelope interface in Class I. The evolution of molecular composition is summarized in Table 5.3.

5.9 Conclusions

In this work we have presented an overview of the molecular tracers of the physical components in protostellar Class 0 and Class I systems. Fig. 5.14 and Table 5.2 present overview of the results and they are summarized below.

- Envelopes are primarily traced by the dense gas tracers $C^{18}O$ and CO snowline tracers such as DCO^+, N_2D^+, $H^{13}CO^+$. For this component, it is essential to use observations that trace large scales of ~ 5000 au.
- Protostellar outflows are separated into different components. High-velocity molecular jets are traced by O-bearing molecules CO, SiO, SO, and H_2CO. Entrained outflow material can be probed by low-velocity CO, SiO, SO, H_2CO, HCN as well as molecules released from ices by sputtering, such CH_3OH, CH_3CHO, HNCO, H_2CCO, CH_3CN, and CH_3OCHO.
- Outflow cavity walls are pronounced in UV-tracers: C_2H, c-C_3H_2, and CN, and high-density tracers such as ^{13}CS.
- Hot cores, the inner warm envelopes, are probed predominantly by COMs but also by simple products released from ice mantles and produced by high-temperature chemistry such as SO, H_2S, H_2CS, OCS, $H^{13}CN$, HCOOH, and HNCO.
- Embedded disks, which are most clearly seen in Class I sources, can be traced by $C^{17}O$ and H_2CO while their upper layers are also traced by CN. SO may probe envelope accretion streams or shocks onto the disk. CO isotopologues can be used to probe disks in Class 0 sources, however, the confusion with the envelope emission requires a detailed analysis of the kinematics to confirm that a Keplerian disk is present.

Hydrocarbons and COMs are found to routinely co-exist in protostellar sources: the former are present in the UV-irradiated cavity walls and the latter in the hot core and in the outflows. It is plausible that PDR chemistry for the formation of hydrocarbons is sufficient to explain the presence of molecules such as C_2H and c-C_3H_2, and that no warm carbon chain chemistry is required which relies on abundant CH_4 in ices. Observations of more complex carbon chains in cavity walls and envelopes is necessary to understand whether the WCCC plays a role there. *JWST* will be able to probe the CH_4 ice content, which will show if any inherent differences in the ice composition between sources.

Throughout this study, the availability of both low-lying molecular lines to probe the cold extended envelope and outflow, as well as high-excitation lines to trace compact hot cores, has been key for the analysis. The occurrence of the same molecules in different physical components then provides an opportunity to study the processes involved in their formation and excitation. For example, ice mantle tracers sputtered from the grains in outflows give useful insight on the ice composition, whereas comparison with abundances of thermally released COMs in the inner region is a powerful tool to probe whether gas-phase formation routes contribute to complex molecule formation.

JWST-MIRI will provide unprecedented resolution and sensitivity in mid-IR that will allow to probe the emission from hot gas in shocks as well as ice absorption features. This can then be combined with our understanding of the kinematics and spatial origin of molecules revealed by ALMA.

Acknowledgements: This paper makes use of the following ALMA data:
ADS/JAO.ALMA#2017.1.01350.S, ADS/JAO.ALMA#2017.1.1174.S,

ADS/JAO.ALMA#2017.1.1371.S, ADS/JAO.ALMA#2017.1.1413.S, ADS/JAO.ALMA#2013.1.00726.S, and ADS/JAO.ALMA#2016.1.00710.S. ALMA is a partnership of ESO (representing its member states), NSF (USA) and NINS (Japan), together with NRC (Canada), MOST and ASIAA (Taiwan), and KASI (Republic of Korea), in cooperation with the Republic of Chile. The Joint ALMA Observatory is operated by ESO, AUI/NRAO and NAOJ. Astrochemistry in Leiden is supported by the Netherlands Research School for Astronomy (NOVA), by a Royal Netherlands Academy of Arts and Sciences (KNAW) professor prize, and by the European Union A-ERC grant 291141 CHEMPLAN. This research made use of Astropy, a community-developed core Python package for Astronomy (Astropy Collaboration et al. 2013), http://astropy.org); Matplotlib library (Hunter 2007); NASA's Astrophysics Data System.

Appendix

5.A Continuum images

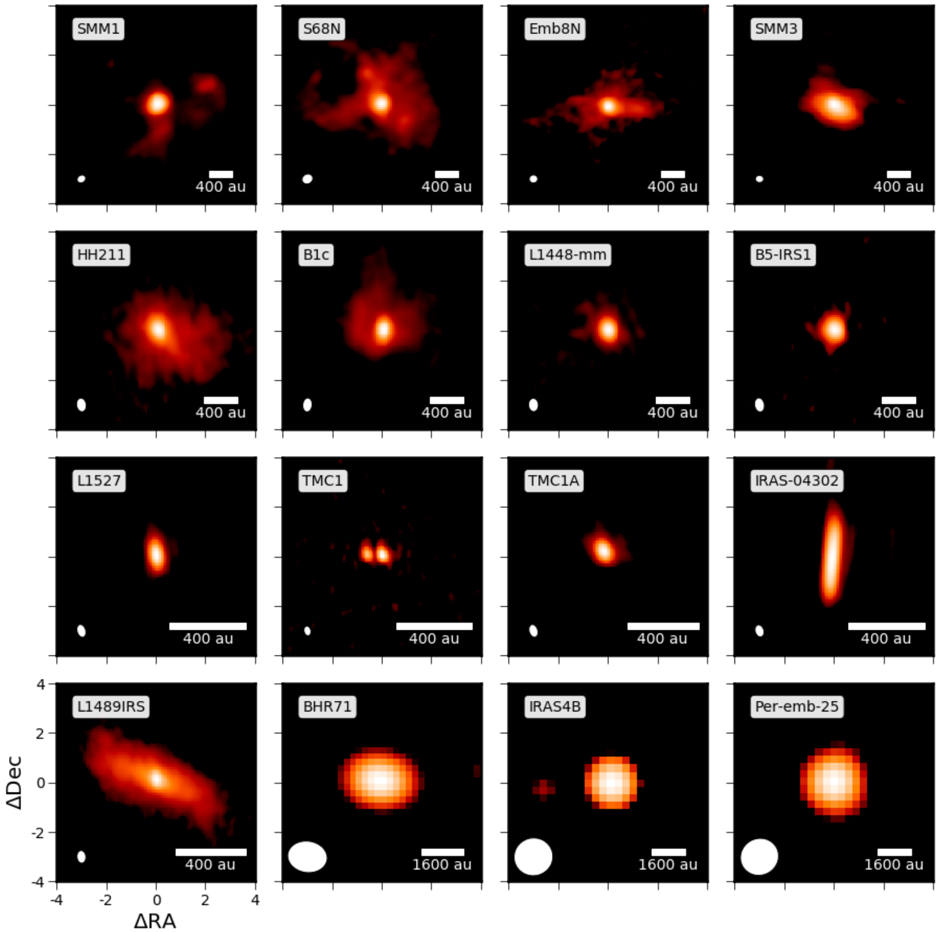

Figure 5.17: Continuum emission from the sources in the sample.

5.B Envelope tracers

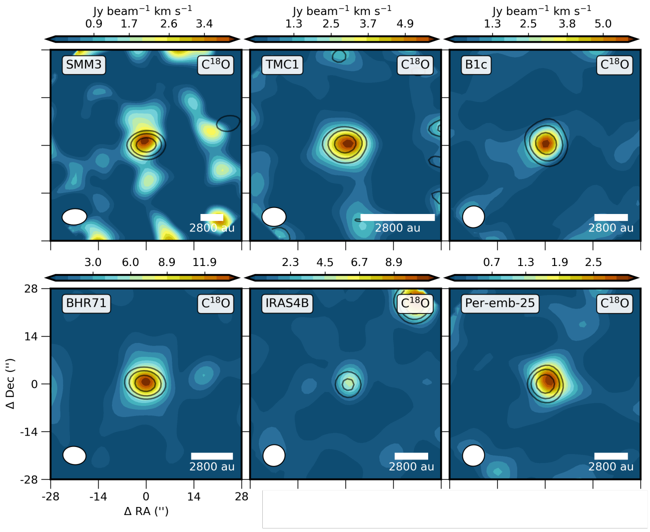

Figure 5.18: Moment maps of $C^{18}O$ at 6″resolution. Contours: continuum, color scale: $C^{18}O$.

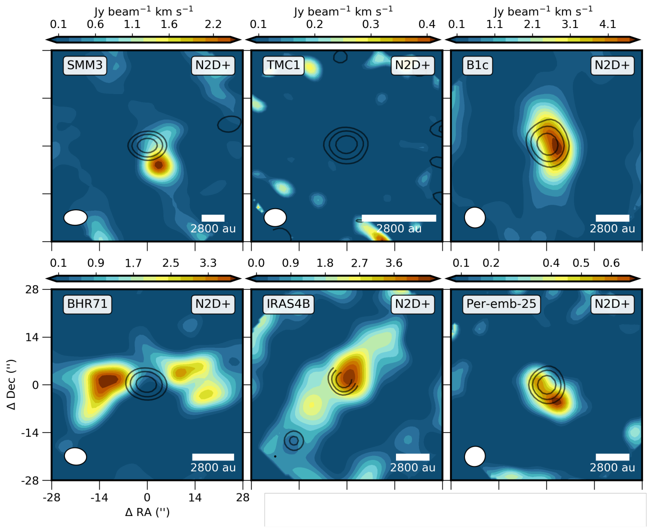

Figure 5.19: Moment maps of N_2D^+ at 6″resolution. Contours: continuum, color scale: moment 0 map integrated from -2 to 2 km s^{-1} w.r.t v_{sys}

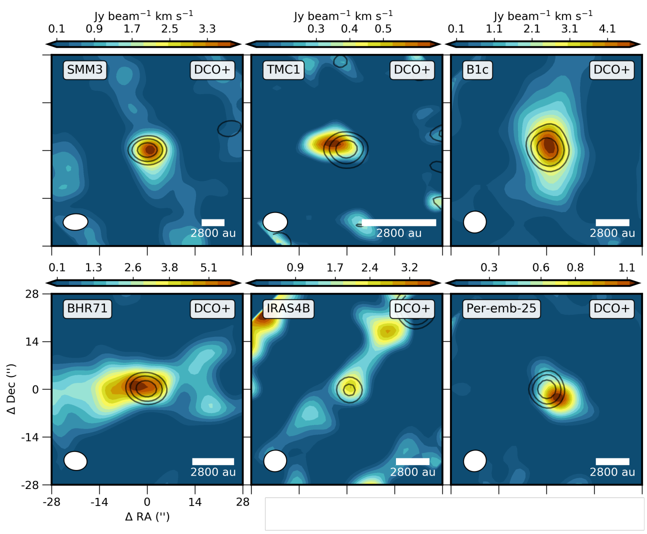

Figure 5.20: Moment maps of DCO^+ at 6″resolution. Contours: continuum, color scale: moment 0 map integrated from -2 to 2 km s^{-1} w.r.t v_{sys}

5.C Outflow

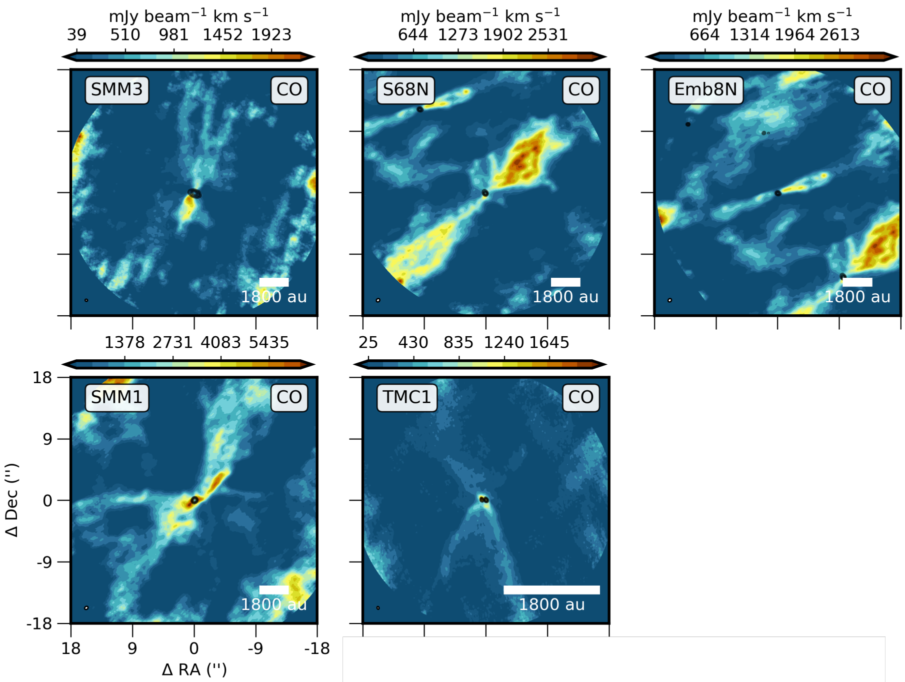

Figure 5.21: Moment maps of low-velocity CO outflow at 0.″4 resolution. Contours: continuum, color scale: moment 0 map integrated from -10 to 10 km s^{-1} w.r.t v_{sys}

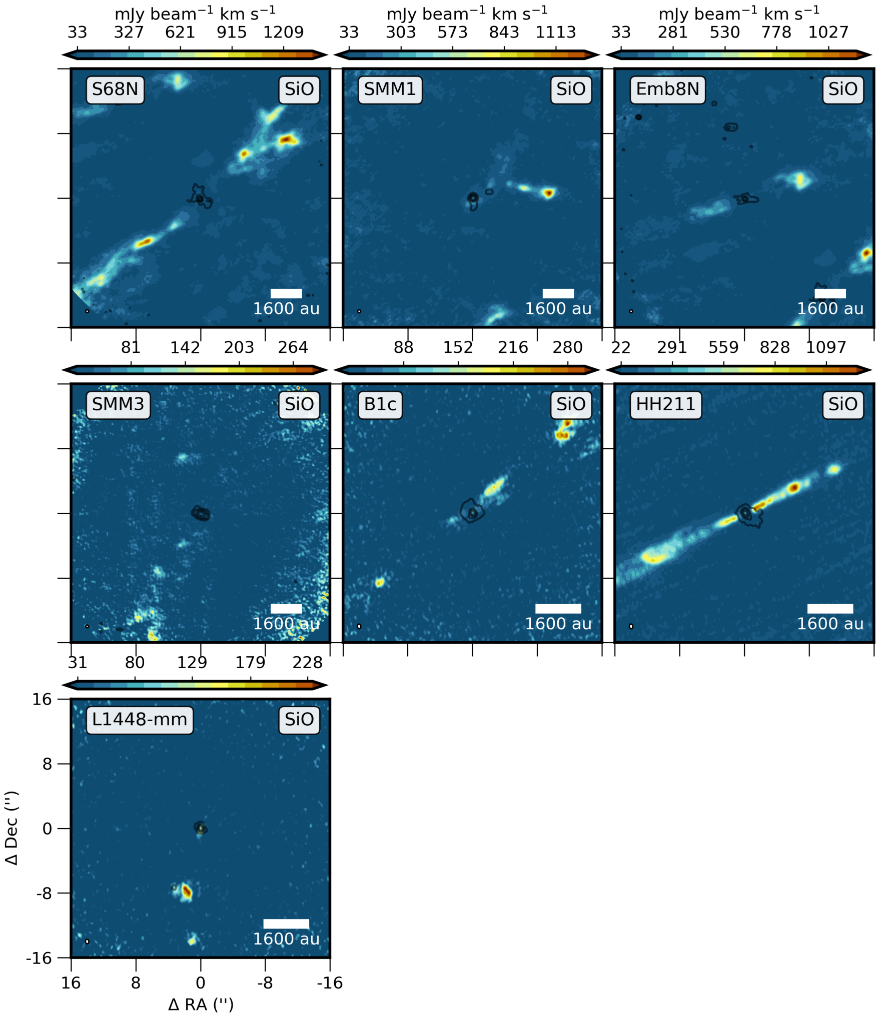

Figure 5.22: Moment maps of low-velocity SiO outflow at 0.″4 resolution. Contours: continuum, color scale: moment 0 map integrated from -15 to 15 km s^{-1} w.r.t v_{sys}

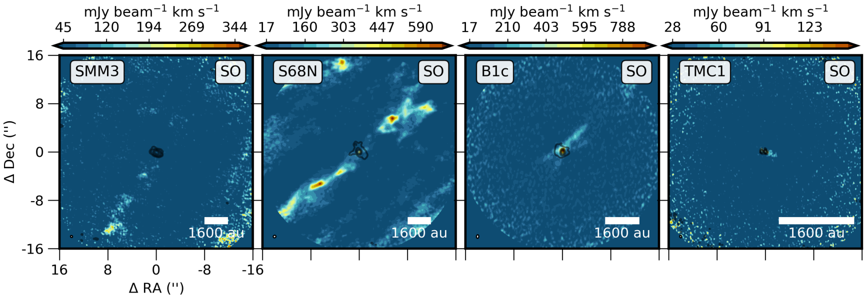

Figure 5.23: Moment maps of low-velocity SO outflow at 0.″4 resolution. Contours: continuum, color scale: moment 0 map integrated from -10 to 10 km s^{-1} w.r.t v_{sys}

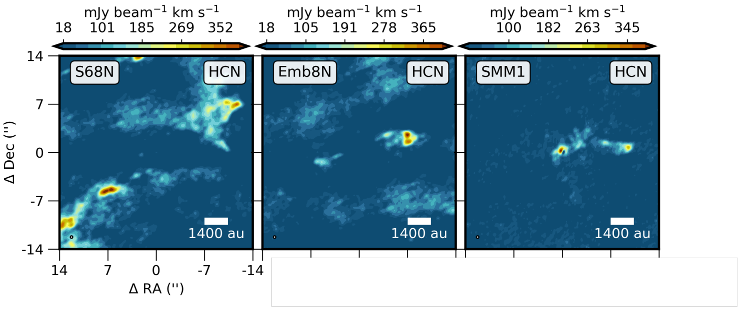

Figure 5.24: Moment maps of HCN at 0.″5 resolution. Color scale: moment 0 map integrated from -15 to 15 km s^{-1} w.r.t v_{sys}

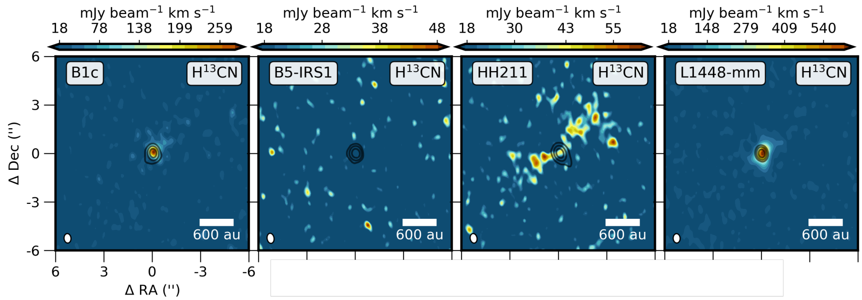

Figure 5.25: Moment maps of H^{13}CN at 0.″4 resolution. Contours: continuum, color scale: moment 0 map integrated from -7 to 7 km s^{-1} w.r.t v_{sys}

5.D Cavity walls

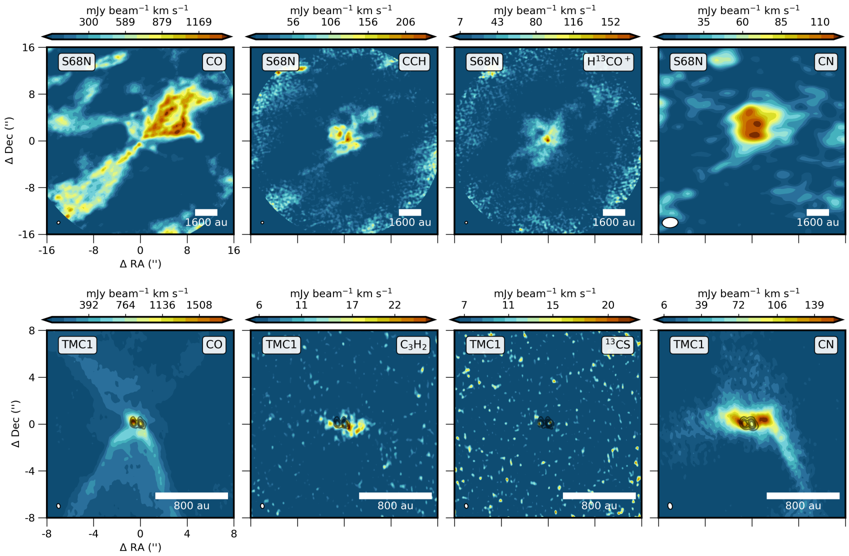

Figure 5.26: Maps of the outflow cavity wall tracers toward S68N and TMC1, with the CO low-velocity outflow map for reference. *Top:* Moment 0 maps toward S68N of CO, C_2H, H_13CO^+ obtained in Band 6 at 0.″5 resolution and CN in Band 3 at 3″. *Bottom:* Moment 0 maps toward TMC1 of CO, c-C_3H_2 and ^{13}CS and CN obtained at 0.″5. The emission is integrated from -5 to -1 km s^{-1} and from 1 to 5 km s^{-1} w.r.t v_{sys}.

5.E Additional plots

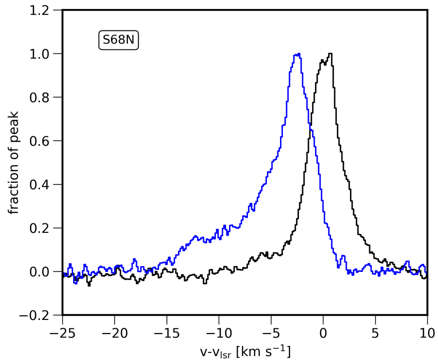

Figure 5.27: Spectra of SO 6_7–5_6 for S68N. Spectra averaged over the 0″.6 diameter circle on positions: central source (black), blueshifted outflow (blue). Both spectra normalized to the peak emission at the position

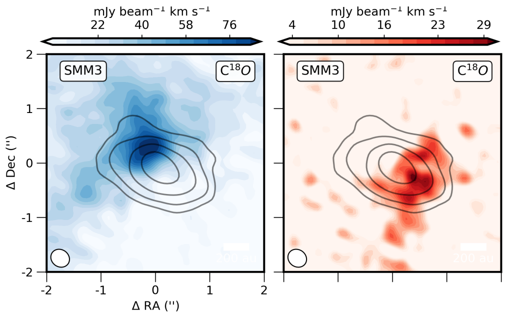

Figure 5.28: Map of the C^{18}O emission toward SMM3. Moment 0 map in colourscale and 1.3 mm continuum in contours. *Left:* Moment 0 map integrated from -3 to -0.5 km s^{-1} w.r.t v_{sys}. *Right:* Moment 0 map integrated from 0.5 to 3 km s^{-1} w.r.t v_{sys}.

5.F Tables

Table 5.4: Specifications of observations

Project ID	Configuration	λ	Res.	MRS	Calibration[a]	Bandpass	Phase	Flux	Targets
2017.1.1350.S	Band 6 (C-4)	1.3 mm	$0\farcs40 \times 0\farcs29$	$5''$	5.4.0-68	J0423-0120	J0336+3218	J0510+1800	SMM3, TMC1
2017.1.1350.S	Band 6 (7m)	1.3 mm	$6\farcs4 \times 6\farcs1$	$25''$	5.4.0-68	J0423-0120	J0336+3218	J0510+1800	SMM3, TMC1, IRAS4B, BHR71, Emb25, B1c
2017.1.1174.S	Band 6 (C-4)	1.3 mm	$0\farcs58 \times 0\farcs39$	$6''$	5.1.1	J1751+0939	J1830+0619	J1751+0939	B1c, S68N, SMM3
2017.1.1174.S	Band 3 (C-2)	3 mm	$2\farcs8 \times 1\farcs8$	$16''$	5.1.1	J0238+1636	J0336+3218	J0238+1636	B1c, S68N
2017.1.1371.S	Band 5 (C-5)	2 mm	$0\farcs6 \times 0\farcs4$	$4''$	5.1.1	J0237+2848	J0336+3218	J0237+2848	L1448, B1c, B5IRS1, HH211
2017.1.1413.S	Band 6 (C-4)	1.3 mm	$0\farcs42 \times 0\farcs28$	$6''$	5.4.0	J0510+1800	J0438+3004	J0510+1800	TMC1, 04302, L1527, TMC1A, L1489
2013.1.00726.S	Band 6 (C-4, C-2)	1.3 mm	$0\farcs45 \times 0\farcs35$	$10''$	4.2.2	J1733-1304	J1751+0939	Titan	SMM1, S68N, Emb8N
2016.1.00710.S	Band 3 (C-5)	3 mm	$0\farcs5 \times 0\farcs4$	$7''$	4.7.38335	J1751+0939	J1838+0404	J1838+0404	SMM1, S68N, Emb8N

Notes. [a] Version of CASA used for calibration

Table 5.5: Molecular transitions targeted

Molecule	Transition	Frequency GHz	E_{up} K	A_{ij} s^{-1}	Serpens S68N	SMM3	SMM1	8N	Perseus B1c	L1448	HH211	B5	Taurus 04302	TMC1	TMC1A	L1527	L1489
CO	$2-1$	230.5380	16.6	6.91e-07	✓	✓	✓	✓	–	–	–	–	–	✓	–	–	–
$C^{18}O$	$2-1$	219.5604	15.8	6.01e-07	–	✓	–	–	–	–	–	–	–	✓	–	–	–
^{13}CO	$2-1$	220.3987	15.9	6.07e-07	✓	✓	✓	✓	–	–	–	–	–	✓	–	–	–
$C^{17}O$	$2_{1.5}-1_{1.5}$	224.7147	16.2	4.50e-07	–	–	–	–	–	–	–	–	✓	✓	✓	✓	✓
$H^{13}CO^+$	$1-0$	86.7543	4.2	3.85e-05	–	–	✓	–	–	–	–	–	–	–	–	–	–
	$2-1$	173.5067	12.5	3.70e-04	–	–	–	–	✓	✓	✓	✗	–	–	–	–	–
	$3-2$	260.2553	25.0	1.34e-03	✓	–	–	✓	✓	–	–	–	–	–	–	–	–
H_2CO	$9_{1,8}-9_{1,9}$	216.5687	174.0	7.22e-06	–	✗	–	–	–	–	–	–	–	✗	–	–	–
	$3_{0,3}-2_{0,2}$	218.2222	21.0	2.82e-04	✗	–	✗	✗	–	–	–	–	–	–	–	–	–
	$3_{2,1}-2_{2,0}$	218.7601	68.1	1.58e-04	–	✓	–	–	–	–	–	–	–	✓	–	–	–
	$3_{1,2}-2_{1,1}$	225.6978	33.5	2.77e-04	–	–	–	–	–	–	–	–	✓	✓	✓	✓	✓
H_2CS	$5_{1,4}-4_{1,3}$	174.3452	38.3	7.32e-05	–	–	–	–	✓	✓	✗	✓	–	–	–	–	–
	$7_{0,7}-6_{0,6}$	240.2669	46.1	2.05e-04	–	–	–	–	–	–	–	–	✓	✗	✓	✗	✗
SO	5_6-4_5	219.9494	35.0	1.36e-04	–	✓	–	–	–	–	–	–	–	✓	–	–	–
	6_7-5_6	261.8437	47.6	2.33e-04	✓	–	–	✓	✓	–	–	–	–	–	–	–	–
SiO	$4-3$	173.6883	20.8	2.61e-04	–	–	–	–	✓	✓	✓	✗	–	–	–	–	–
	$5-4$	217.1050	31.3	5.21e-04	✓	✓	✓	✓	–	–	–	–	–	✗	–	–	–
DCO^+	$3-2$	216.1126	20.7	7.61e-04	✓	✓	✓	✓	–	–	–	–	–	✓	–	–	–
N_2D^+	$3-2$	231.3218	22.2	7.14e-04	–	✓	–	–	–	–	–	–	–	✗	–	–	–
OCS	1_9-1_8	231.0610	110.9	3.58e-05	–	✓	–	–	–	–	–	–	–	✗	–	–	–
HNCO	$5_{0,5}-4_{0,4}$	109.9058	15.8	1.80e-05	✓	–	–	✗	✓	–	–	–	–	–	–	–	–
	$11_{0,11}-10_{0,10}$	241.7741	69.6	2.00e-04	–	–	–	–	–	–	–	–	✗	✗	✗	✗	✓
	$12_{1,12}-11_{1,11}$	262.7696	125.3	2.57e-04	✓	–	–	✗	✓	–	–	–	–	–	–	–	–
	$12_{0,12}-11_{0,11}$	263.7487	82.3	2.61e-04	✓	–	–	✗	✓	–	–	–	–	–	–	–	–
	$12_{1,12}-11_{1,11}$	262.7751	125.1	2.57e-04	✓	–	–	✗	✓	–	–	–	–	–	–	–	–
H_2CCO	$13_{1,13}-12_{1,12}$	260.1920	100.5	1.98e-04	✓	–	–	–	✓	–	–	–	–	–	–	–	–
	$13_{2,11}-12_{2,10}$	262.7609	140.5	2.01e-04	✓	–	–	✗	✓	–	–	–	–	–	–	–	–
HCOOH	$12_{0,12}-11_{0,11}$	262.1036	82.8	1.95e-04	✓	–	–	✗	✓	–	–	–	–	–	–	–	–
	$5_{0,5}-4_{0,4}$	111.7468	16.1	1.44e-05	✗	–	–	✗	✓	–	–	–	–	–	–	–	–
	$5_{2,4}-4_{2,3}$	112.2871	28.9	1.23e-05	✗	–	–	✗	✓	–	–	–	–	–	–	–	–
^{13}CS	$5-4$	231.2207	33.3	2.51e-04	✓	✓	✓	✓	–	–	–	–	–	✓	–	–	–
CN	$1_{0,0.5,0.5}-0_{0,0.5,1.5}$	113.1442	5.4	1.05e-05	✓	–	–	✓	✓	–	–	–	–	–	–	–	–
	$2_{0,1.5,2.5}-1_{0,1.5,2.5}$	226.3599	16.3	1.61e-05	–	–	–	–	–	–	–	–	✗	✓	✓	✓	✓
	$2_{0,1.5,0.5}-1_{0,0.5,1.5}$	226.6166	16.3	1.07e-05	–	–	–	–	–	–	–	–	✗	✓	✗	–	✓
	$2_{0,1.5,1.5}-1_{0,0.5,1.5}$	226.6322	16.3	4.26e-05	–	–	–	–	–	–	–	–	✓	✓	✓	✓	✓
	$2_{0,1.5,2.5}-1_{0,0.5,1.5}$	226.6596	16.3	9.47e-05	–	–	–	–	–	–	–	–	✓	✓	✓	✓	✓
	$2_{0,1.5,0.5}-1_{0,0.5,0.5}$	226.6637	16.3	8.46e-05	–	–	–	–	–	–	–	–	✓	✓	✓	✓	✓
	$2_{0,1.5,1.5}-1_{0,0.5,0.5}$	226.6793	16.3	5.27e-05	–	–	–	–	–	–	–	–	✓	✓	✓	✓	✓
	$2_{0,2.5,2.5}-1_{0,1.5,1.5}$	226.8742	16.3	9.62e-05	–	–	–	–	–	–	–	–	✓	✓	✓	✓	✓
	$2_{0,2.5,3.5}-1_{0,1.5,2.5}$	226.8748	16.3	1.14e-04	–	–	–	–	–	–	–	–	✓	✓	✓	✓	✓
	$2_{0,2.5,1.5}-1_{0,1.5,0.5}$	226.8759	16.3	8.59e-05	–	–	–	–	–	–	–	–	✓	✓	✓	✓	✓
	$2_{0,2.5,1.5}-1_{0,1.5,1.5}$	226.8874	16.3	2.73e-05	–	–	–	–	–	–	–	–	✓	✓	✓	✓	✓

Table 5.5: Continued.

Molecule	Transition	Frequency GHz	E_{up} K	A_{ij} s^{-1}	Serpens S68N	SMM3	SMM1	8N	Perseus B1c	L1448	HH211	B5	Taurus 04302	TMC1	TMC1A	L1527	L1489
	$2_{0,2.5,2.5}-1_{0,1.5,2.5}$	226.8921	16.3	1.81e-05	–	–	–	–	–	–	–	–	✓	✓	✓	✓	✓
HCN	1_1-0_1	88.6304	4.3	2.43e-05	✓	–	✓	✓	–	–	–	–	–	–	–	–	–
	1_2-0_1	88.6318	4.3	2.43e-05	✓	–	✓	✓	–	–	–	–	–	–	–	–	–
	1_0-0_1	88.6339	4.3	2.43e-05	✓	–	✓	✓	–	–	–	–	–	–	–	–	–
$H^{13}CN$	1_0-0_1	86.3423	4.1	2.22e-05	✓	–	✓	✓	–	–	–	–	–	–	–	–	–
	2_2-1_2	172.6766	12.4	5.34e-05	–	–	–	–	✓	✓	✓	✗	–	–	–	–	–
	2_1-1_2	172.6779	12.4	5.93e-06	–	–	–	–	✓	✓	✓	✓	–	–	–	–	–
	2_2-1_1	172.6780	12.4	1.60e-04	–	–	–	–	✓	✓	✓	✗	–	–	–	–	–
CCH	$3_{2.5,2}-2_{1.5,2}$	262.0788	25.2	6.49e-06	✓	–	–	✗	✓	–	–	–	–	–	–	–	–
	$3_{2.5,3}-2_{1.5,2}$	262.0648	25.2	5.28e-05	✓	–	–	✓	✓	–	–	–	–	–	–	–	–
	$3_{2.5,2}-2_{1.5,1}$	262.0673	25.2	4.83e-05	✓	–	–	✓	✓	–	–	–	–	–	–	–	–
	$3_{3.5,3}-2_{2.5,2}$	262.0064	25.1	5.52e-05	✓	–	–	✓	✓	–	–	–	–	–	–	–	–
	$3_{3.5,4}-2_{2.5,3}$	262.0042	25.1	5.74e-05	✓	–	–	✓	✓	–	–	–	–	–	–	–	–
c-C_3H_2	$7_{4,3}-7_{3,4}$	112.4908	82.6	4.50e-05	✓	✓	–	✓	✓	–	–	–	–	–	–	–	–
	$6_{1,6}-5_{0,5}$	217.8221	38.6	5.93e-04	–	✓	–	–	–	–	–	–	–	✓	–	–	–
	$7_{2,6}-7_{1,7}$	218.7327	61.2	9.82e-05	–	✓	–	–	–	–	–	–	–	✓	–	–	–
	$3_{3,1}-2_{0,2}$	261.8318	19.0	4.66e-05	–	–	–	–	✓	–	–	–	–	–	–	–	–
CH_3CHO	$6_{1,6}-5_{1,5}$	112.2545	21.2	4.50e-05	✓	✓	–	✗	–	–	–	–	–	–	–	–	–
	$9_{4,5}-8_{4,4}$	173.5191	77.7	1.41e-04	–	–	–	–	✓	✓	✗	✗	–	–	–	–	–
	$14_{0,14}-13_{0,13}$	262.9601	95.8	6.20e-04	✓	–	–	–	✓	–	–	–	–	–	–	–	–
	$14_{0,14}-13_{0,13}$	263.0040	95.7	6.20e-04	✓	–	–	–	✓	–	–	–	–	–	–	–	–
CH_3CN	6_0-5_0	110.3835	18.5	1.11e-04	✓	✓	–	✓	✓	–	–	–	–	–	–	–	–
	6_4-5_4	110.3495	132.8	6.17e-05	✓	–	–	–	✓	–	–	–	–	–	–	–	–
	6_3-5_3	110.3644	82.8	8.33e-05	✓	✓	–	✓	✓	–	–	–	–	–	–	–	–
	6_2-5_2	110.3750	47.1	9.87e-05	✓	✓	–	✓	✓	–	–	–	–	–	–	–	–
	6_1-5_1	110.3814	25.7	1.08e-04	✓	✓	–	✓	✓	–	–	–	–	–	–	–	–
CH_3OH	$4_{2,3}-5_{1,4}$	234.6834	60.9	1.85e-05	–	✗	–	–	–	–	–	–	–	✗	–	–	–
	$5_{-1}-4_{-1}$	241.7672	40.4	5.81e-05	–	–	–	–	✓	–	–	–	–	✗	–	–	–
	5_0-4_0	241.7914	34.8	6.05e-05	–	–	–	–	–	–	–	–	–	✗	–	✓	✓
	5_2-4_2	241.9046	57.1	5.03e-05	–	–	–	–	–	–	–	–	–	✗	✓	✓	–
	$2_{1,0}-1_{0,1}$	261.8057	28.0	5.57e-05	✓	–	–	✓	✓	–	–	–	–	–	–	–	–
CH_3OCHO	$9_{5,5}-8_{5,4}$	110.8823	43.2	1.38e-05	✓	–	–	–	✓	–	–	–	–	–	–	–	–
	$10_{0,10}-9_{0,9}$	111.1699	30.2	1.99e-05	✓	✗	–	✗	✓	–	–	–	–	–	–	–	–
	$9_{1,8}-8_{1,7}$	111.6741	28.1	1.98e-05	✓	✗	–	✗	✓	–	–	–	–	–	–	–	–

Notes. ✓- transition detected, ✗- transition not detected, – transition not targeted